

1 **Observation of quiet-time mid-latitude Joule heating**
2 **and comparisons with the TIEGCM simulation**

3 **E. K. Day¹, A. Grocott¹, M.-T. Walach¹, J. A. Wild¹, G. Lu², J. M.**
4 **Ruohoniemi³, A. J. Coster⁴**

5 ¹Lancaster University, Lancaster, United Kingdom

6 ²National Center for Atmospheric Research, High Altitude Observatory, Boulder, CO, United States

7 ³Virginia Polytechnic Institute and State University, Blacksburg, United States

8 ⁴MIT Haystack Observatory, Westford, United States

9 **Key Points:**

- 10 • Observations from an FPI and SuperDARN radar were used to estimate quiet-
11 time mid-latitude Joule heating rates during 16 July 2014.
- 12 • The neutral winds accounted for between 24% to 43% of the total observed local
13 Joule heating rates.
- 14 • Joule heating enhancements were observed approximately 8 times higher than mod-
15 elled by TIEGCM due to excitations in sub-auroral ion motion.

Corresponding author: E. K. Day, e.day1@lancaster.ac.uk

Abstract

Joule heating is a major energy sink in the solar wind-magnetosphere-ionosphere system and modelling it is key to understanding the impact of space weather on the neutral atmosphere. Ion drifts and neutral wind velocities are key parameters when modelling Joule heating, however there is limited validation of the modelled ion and neutral velocities at mid-latitudes. We use the Blackstone Super Dual Auroral Radar Network (SuperDARN) radar and the Michigan North American Thermosphere Ionosphere Observing Network (NATION) Fabry-Perot interferometer (FPI) to obtain the local nighttime ion and neutral velocities at $\sim 40^\circ$ geographic latitude during the nighttime of 16 July 2014. Despite being a geomagnetically quiet period, we observe significant sub-auroral ion flows in excess of 200ms^{-1} . We calculate an enhancement to the local Joule heating rate due to these ion flows and find that the neutrals impart a significant increase or decrease to the total Joule heating rate of $> 75\%$ depending on their direction. We compare our observations to outputs from the Thermosphere Ionosphere Electrodynamics General Circulation Model (TIEGCM). At such a low geomagnetic activity however, TIEGCM was not able to model significant sub-auroral ion flows and any resulting Joule heating enhancements equivalent to our observations. We found that the neutral winds were the primary contributor to the Joule heating rates modelled by TIEGCM rather than the ions as suggested by our observations.

Plain Language Summary

Charged particle motion in Earth's upper atmosphere creates heating called Joule heating which causes the atmosphere to expand, increasing drag for objects and satellites. Charged particle velocities are typically greater at high-latitudes than mid and lower latitudes. At mid and lower latitudes, Earth's neutral atmosphere can move faster than the charged particles and produce Joule heating. We can use ground based instruments to observe this particle motion and estimate the Joule heating. Physical models can estimate the Joule heating for different space weather conditions. These physical models show good estimations of the high-latitude Joule heating compared to estimations, however there is limited validation of their performance at mid-latitudes.

We use ground based instruments to estimate the Joule heating over mid-latitude North America for one night and compare to outputs from a physics model called TIEGCM. Despite quiet driving conditions, we observe significant charged particle motion driving enhanced Joule heating rates. We find that TIEGCM was unable to model these strong charged particle motions nor any Joule heating enhancements equivalent to our observations. While the observed heating resulted from faster charged particle motion, the Joule heating rates in TIEGCM were produced by the greater neutral winds instead of ion drifts.

1 Introduction

A significant fraction of the energy flowing through the magnetosphere-ionosphere system is lost to the atmosphere via Joule heating, which in the ionosphere-thermosphere system can be equated to frictional heating between charge carriers and neutral constituents within Earth's upper atmosphere (Vasyliunas & Song, 2005). Joule heating is the dominant magnetosphere-ionosphere energy input source, typically responsible for twice as much energy input compared to auroral power (Lu et al., 1996, 1998; Knipp et al., 2004; Lu et al., 2016) and up to 70% of the total ionospheric power input during geomagnetic storms (Knipp et al., 2004). This heating can cause ionospheric and thermospheric expansion (Rishbeth et al., 1969; Fuller-Rowell et al., 1997; Knipp et al., 1998; Lu et al., 2016; S. R. Zhang et al., 2017) which can result in enhanced ion outflow (Wahlund et al., 1992) and increased satellite drag that can reduce operational lifetime (Dang et al.,

2022; Fang et al., 2022; Lin et al., 2022). It is therefore important that we understand the causes of Joule heating across all regions of the ionosphere.

Joule heating has been extensively studied at the high-latitudes (Kiene et al., 2019; Wang et al., 2020). Ion motion is controlled by magnetic reconnection between the interplanetary magnetic field (IMF) and Earth’s magnetosphere, circulating due to $\vec{E} \times \vec{B}$ drift antisunwards at polar latitudes then returning sunwards at lower latitudes (Dungey, 1961; Cowley & Lockwood, 1992) under southwards IMF conditions. Motion of the neutrals in the thermosphere is driven by a combination of solar pressure gradients, coriolis forces and drag from ion motion (Rishbeth, 1977). Typically at high-latitudes, neutral velocities are small relative to the ion velocities such that Joule heating is primarily due to motion of the ions. High-latitude Joule heating calculations have therefore often discounted contributions from the neutrals. However during non-storm times and at lower latitudes, the velocities of the neutrals relative to the ions can be significant. Using model simulations, Lu et al. (1995) calculated the neutrals to have an approximate 28% negative effect on Joule heating. Often the neutral velocities at mid-latitudes can exceed the ion velocities. Both Zou and Nishitani (2014) and Joshi et al. (2015) used Super Dual Auroral Radar Network (SuperDARN) data to show that neutral motion driven by expanded $\vec{E} \times \vec{B}$ ion drift due to intense geomagnetic storms can persist up to 20 hours after the recovery phase, resulting in neutral wind driven mid-latitude ion motion known as the disturbance dynamo effect. A study by Billett et al. (2018) focusing on the high-latitudes used a combination of SuperDARN and neutral wind model data to find that global Joule heating patterns have a significant dependence on UT due to neutral wind enhancements. Studies including the mid-lower latitudes and during periods of weaker geomagnetic activity must therefore include neutral wind contributions when calculating the Joule heating.

Joule heating is calculated as the dissipation rate of currents perpendicular to the magnetic field, $\vec{J}_\perp \cdot \vec{E}$ (Lu et al., 1995) and the total Joule heating rate can be calculated with equation (1) (Baker et al., 2004),

$$\vec{J}_\perp \cdot \vec{E}_\perp = \sigma_p (\vec{E} + \vec{V}_n \times \vec{B})^2 \quad (1)$$

where $\vec{E} = -\vec{V}_i \times \vec{B}$ is the electric field in the Earth’s reference frame due to the ion motion, \vec{V}_i , assuming a stationary neutral background, σ_p is the conductivity in the direction of the electric field (Pedersen conductivity), V_n is the velocity of the background neutrals and \vec{B} is the magnetic field strength. $\vec{V}_n \times \vec{B}$ accounts for the electric field generated by the neutral wind dynamo due to the drag imposed on charged particles in the ionosphere.

Equation 1 can be expanded into equation 2 (Billett et al., 2018) which conveniently breaks it down into the three terms that individually describe the main contributors to the total Joule heating.

$$Q_j = \underbrace{\sigma_p E^2}_{Q_i} + \underbrace{2\sigma_p \vec{E} \cdot (\vec{V}_n \times \vec{B})}_{Q_{w1}} + \underbrace{\sigma_p (\vec{V}_n \times \vec{B})^2}_{Q_{w2}} \quad (2)$$

Q_i is the ion heating and is the heating that would be generated by ions moving against a stationary neutral background. Q_{w1} is the 1st wind correction term and accounts for the direction of the ions relative to the neutrals. If the neutrals and ions move in the same direction then the difference between their velocities is smaller and the frictional heating due to collisions between the neutrals and ions will be lower. Conversely, if they move in opposing directions the difference in their velocities will be greater and

108 the heating will be larger, therefore Q_{w1} can act to either increase or decrease the to-
 109 tal Joule heating. Q_{w2} is the heating that would be generated by the neutrals moving
 110 against a stationary ion background. Together, Q_{w1} and Q_{w2} create the wind correction
 111 term Q_w , which describes the total heating accounted for by motion of the neutral wind
 112 relative to the ions.

113 Except for geomagnetic storms, where the twin cell $\vec{E} \times \vec{B}$ convection pattern ex-
 114 pands to 40° magnetic latitude (Walach & Grocott, 2019; Walach et al., 2021) from its
 115 high-latitude ($> 60^\circ$ magnetic latitude) boundary, most ion flows at the mid-latitudes
 116 ($40^\circ - 60^\circ$ magnetic latitude) are sub-auroral. At sub-auroral latitudes, ion motion is
 117 often associated with sub-auroral polarization streams (SAPS) (Clausen et al., 2012; Bil-
 118 lett et al., 2022), penetrating electric fields (Maimaiti et al., 2018, 2019) and pressure
 119 gradient drifts (Hudson & Kelley, 1976; Greenwald et al., 2006; Liu et al., 2021) that are
 120 mostly responsible for driving subauroral ion flows. Billett et al. (2022) observed signif-
 121 icant equatorward and westward neutral wind disturbances during a SAPS event. They
 122 found that the response of the neutrals close to the SAPS was almost immediate and was
 123 likely driven by ion neutral coupling. They did however also find neutral disturbances
 124 further from the SAPS after a 2 hour time lag that they propose were due to pressure
 125 gradient and Coriolis forces from the SAPS heating. The difference in neutral response
 126 due to location indicates the importance of considering the mesoscale structure of iono-
 127 spheric events when accounting for neutral particle motion. Furthermore a study by Kiene
 128 et al. (2019) found that the difference in high-latitude Joule heating rates varied by as
 129 much as a factor of 10 due to local variations in the observed ion-neutral structure. If
 130 we are to accurately estimate the Joule heating rate during ionosphere-thermosphere dis-
 131 turbances it is then necessary to ensure that the ion and neutral measurements are as
 132 colocated as possible.

133 The Blackstone (BKS) Super Dual Auroral Radar Network (SuperDARN) radar
 134 and the Ann Arbor (ANN) North American Thermosphere Ionosphere Observation Net-
 135 work (NATION) interferometer are two mid-latitude ground-based instruments, used for
 136 observing ion and neutral flows in the F-region of the ionosphere respectively, (see sec-
 137 tion 2) whose fields of view (FOV's) overlap each other, allowing for colocated observa-
 138 tions of mid-latitude ion and neutral flows. As the majority of ion motion at the mid-
 139 latitudes occur during quiet periods we search for quiet time coincident ion and neutral
 140 observations. Identifying times of high-quality colocated observations during quiet times
 141 is extremely difficult. Both instruments need to be operational, the BKS radar needs to
 142 observe ionospheric scatter during the nighttime period in the region over the FPI and
 143 the ANN FPI needs to have suitable (uncloudy) observation conditions. Intervals where
 144 all these requirements are satisfied are unfortunately rare. Nevertheless we have iden-
 145 tified the nighttime of 16 July 2014 as a period where all the necessary conditions are
 146 met, allowing us to study the local quiet-time mid-latitude Joule heating during this in-
 147 terval.

148 Global circulation models are often used to study high-latitude ionosphere-thermosphere
 149 and Joule heating processes (Lu et al., 2016; Wang et al., 2020), however a lack of stud-
 150 ies using global models focused on the mid-latitudes leaves some uncertainty in their re-
 151 liability to provide accurate mid-latitude modelling. We therefore compare our ion and
 152 neutral observations and Joule heating estimations with equivalent outputs from the Ther-
 153 mosphere Ionosphere General Circulation Model (TIEGCM, see section 2). This paper
 154 is split into the following sections: Section 2 details the observed and modelled data used
 155 in this study, Section 3 provides an overview of the geomagnetic conditions and obser-
 156 vations made during the night of 16 July 2014. Section 4 details the methods used to
 157 estimate the Joule heating rate while presenting the results of those estimations. Finally,
 158 section 5 discusses the results in context of the wider literature and scientific commu-
 159 nity.

2 Parameters and Models

2.1 Ion Motion

The Super Dual Auroral Radar Network (SuperDARN) (Greenwald et al., 1995; Chisham et al., 2007; Nishitani et al., 2019) is a series of high frequency radars in the northern and southern hemispheres that provide observations of ionospheric dynamics across high and mid-latitudes. In the northern hemisphere, SuperDARN comprises radars which have near total hemispheric coverage of the polar, high-latitude and mid-latitude regions. For this investigation we consider data from the Blackstone (BKS) radar due to its field of view (FOV) overlapping the FPI used in this study (see section 2.2). Each radar can electronically steer its look direction, centred on which it forms a beam typically 3° wide and consisting of 75-100 range gates with a 45km range resolution. Each radar can sweep through 16-24 beams with the FOV being roughly 50° where a full azimuthal scan across all beams takes 1-2 min.

SuperDARN radars detect field-aligned plasma irregularities in the E and F regions of the ionosphere by recording the backscattered signal from decameter scale electron density structures. Plasma irregularities in the F region drift with $\vec{E} \times \vec{B}$ velocities and their Doppler shift can be used to infer properties of the ionosphere. Due to refraction, the radar beam can reflect off of the ground, known as groundscatter. Groundscatter is typically characterised by a velocity of only a few ms^{-1} and produces a low spectral width, which is often sufficient to distinguish between ionospheric and ground scatter at the high-latitudes. At the mid-latitudes however, and particularly during periods of low geomagnetic activity, ionospheric scatter can often be much slower while exhibiting low spectral widths and these techniques can often eliminate observations of relevant ion motion. Instead we use the algorithm developed by Ribeiro et al. (2011, 2012) which has been specifically designed for identifying mid-latitude ionospheric scatter. The algorithm uses a $3 \times 3 \times 3$ beam by range gate by scan boxcar filter that identifies individual clusters of scatter connected by range gate and scan and determines the ratio of fast to slow moving scatter within each cluster. Errors associated with the filtered velocities are derived using the method described by Ruohoniemi and Baker (1998), however we have modified the method so that velocities are removed if they are two median absolute deviations (Howell, 2005) from the median instead of two standard deviations from the mean. This reduces the impact of unphysical outliers that result in excessive standard deviations due to the lower velocities associated with the mid-latitudes. Since an individual cluster of returned scatter can usually be attributed to either ionospheric backscatter or groundscatter, the algorithm identifies and marks which clusters contain ionospheric scatter. The Ribeiro et al. (2011) algorithm also automatically excludes backscatter from ranges within 315km of the radar to eliminate scatter originating from the E-region and meteor echoes at near ranges. Furthermore, in this study we modify the algorithm such that it can consider clusters spanning multiple beams similar to A. G. Burrell et al. (2018). This whole approach enables a quantitative ionospheric/groundscatter classification of mid-latitude backscatter.

2.2 Neutral Wind Motion

The North American Thermosphere Ionosphere Observing Network (NATION) (Makela et al., 2012) was a network of five Fabry-Perot Interferometers that observed the neutral wind velocity and temperature in Earth's thermosphere across the mid and eastern parts of the United States of America. Each FPI observes the Doppler shift of the 630nm OI emission line that is assumed to peak at an altitude of 250km. The FPIs scan at an elevation angle of 45° and take measurements in the geographic cardinal directions (north, east, south, west) and the Zenith through the nighttime period. Data are analyzed using the techniques described in Harding et al. (2014) to produce estimates of the horizontal neutral winds at $\sim 250\text{km}$ altitude.

211 Of the five FPIs in NATION, and assuming that the cardinal measurement loca-
 212 tions are located at the peak emission altitudes, we only use data from the Michigan (ANN)
 213 instrument due to it being the only FPI that has all of its measurement locations inter-
 214 secting with the BKS radar’s FOV.

215 **2.3 Geomagnetic Field**

216 The 13th generation International Geomagnetic Reference Field (IGRF) model (Alken
 217 et al., 2021) profiles the Earth’s tilted dipole as a function of time, geographic position
 218 and altitude. At high-latitudes, the magnetic field is mostly vertical, however at mid-
 219 latitudes and lower, there can be a significant tilt to the angle of the field that needs to
 220 be accounted for when comparing the electric field generated by the neutral wind dy-
 221 namo ($\vec{V}_n \times \vec{B}$) with the electric field that is calculated from $\vec{E} \times \vec{B}$ drift, due to the
 222 difference in angle between the ion and neutral velocity vectors. The IGRF13 model pro-
 223 vides the declination and inclination of the magnetic field at the ANN FPI’s location,
 224 which at 250km altitude are -6.49° and 69.26° respectively. This inclination and dec-
 225 lination do not change significantly between assumed peak emission locations so we do
 226 not consider it in our calculations.

227 **2.4 Auroral Boundary**

228 Due to the mid-latitude location this study focuses on, it is important to identify
 229 if any observed ion flows are sub-auroral. It has been shown that the boundary between
 230 the region 1 and region 2 currents serve as a good approximation for the extent of equa-
 231 torward boundary of the auroral oval, particularly on the duskside in the northern hemi-
 232 sphere (Kilcommons et al., 2017). The Active Magnetosphere and Planetary Electrody-
 233 namics Response Experiment (AMPERE) uses magnetometers on the Iridium constel-
 234 lation of telecommunication satellites to provide field aligned current measurements across
 235 both hemispheres. A spherical harmonic fit to the measured radial current densities along-
 236 side Ampere’s law (B. J. Anderson et al., 2000; Coxon et al., 2018) produces 10-minute
 237 cadence global current density maps which can be used to determine the location of the
 238 Region 1 and 2 currents, where we use the boundary between them as a proxy for the
 239 boundary of the auroral oval.

240 **2.5 Total Electron Content**

241 The mid-latitude ionospheric trough plays a significant role in ionospheric processes
 242 in the mid-latitudes (P. C. Anderson et al., 1993; Kunduri et al., 2021; Liu et al., 2021)
 243 and can be identified using Total Electron Content (TEC) measurements from Global
 244 Positioning System (GPS) data. We use the TEC data to further investigate the mid-
 245 latitude dynamics through identification of the trough. The TEC data are processed us-
 246 ing the algorithms from Rideout and Coster (2006) and Vierinen et al. (2016). The TEC
 247 data are placed into $1^\circ \times 1^\circ$ geographic latitude by geographic longitude cells integrated
 248 over 5 minutes. Furthermore we median filter the TEC data as described by Thomas et
 249 al. (2013) to reduce the geospatial noise among the dataset.

250 **2.6 TIEGCM**

251 The Thermosphere Ionosphere Electrodynamic Circulation Model (TIEGCM) (Richmond
 252 et al., 1992; Qian et al., 2014) is one of the most widely used thermosphere/ionosphere
 253 models within the upper atmospheric scientific community and is a fully three-dimensional
 254 time dependent model of Earth’s ionosphere and thermosphere that solves the equations
 255 of continuity, energy and momentum for the three major ion and neutral species.

256 TIEGCM uses either the Weimer (Weimer, 2005) or Heelis (Heelis et al., 1982) elec-
 257 tric field models as a driver for the $\vec{E} \times \vec{B}$ driven high-latitude ion convection and can

258 operate using a $5^\circ \times 5^\circ$ or $2.5^\circ \times 2.5^\circ$ resolution in latitude and longitude. Wu et al.
 259 (2017) compared TIEGCM's high-latitude thermospheric winds and ion drifts using the
 260 two electric field models to observational data and found that using the Weimer model
 261 produces more accurate simulations. In this study we run TIEGCM with the Weimer
 262 electric field model at a resolution of $2.5^\circ \times 2.5^\circ$. When using the Weimer electric field
 263 model TIEGCM takes the f10.7 solar radio flux, IMF By, IMF Bz, solar wind velocity
 264 and solar wind density as input drivers for the model.

265 TIEGCM produces estimates of the geographic meridional, zonal and vertical ion
 266 and neutral velocities at the specified run resolution. Outputs from TIEGCM in this study
 267 are taken at an altitude of 250km, which corresponds to the altitudes of the ion and neu-
 268 tral observations. As the ion and neutral line of sight velocities show little difference be-
 269 tween assumed peak emission locations, we simply use the TIEGCM ion and neutral ve-
 270 locities located at the FPI location.

271 TIEGCM also models the Pedersen conductivity, which we use for calculating both
 272 the observational and modelled Joule heating values. Keeping the Pedersen conductiv-
 273 ity consistent between observed/modelled methods allows us to better isolate the effect
 274 from differences between the observed and modelled ion and neutral velocities, which is
 275 the aim of this study.

276 3 Event Overview

277 In this section we present observations from 16 July 2014. First we present an overview
 278 of the geomagnetic conditions, before looking in detail at the ion and neutral velocity
 279 observations.

280 3.1 Geomagnetic Conditions

281 Geomagnetic conditions during this interval were quiet. Figure 1 shows the inter-
 282 planetary and geomagnetic conditions, IMF By, IMF Bz, SYM-H, ASYM-H and Kp dur-
 283 ing the hours 0000-1000 UT. Panel 1a shows the solar wind speed while 1b presents the
 284 y and z components of the IMF. Of particular note is the slight negative IMF Bz between
 285 0400 and 0700 UT indicating a southwards directed IMF, allowing magnetic reconnec-
 286 tion to occur between the IMF and Earth's magnetic field. Panel 1c shows the auroral
 287 indices with significant enhancements to the AL, AU and derived AE index coincident
 288 with the period of southwards IMF, indicating an increased intensity of the auroral elec-
 289 trojet. Similarly, the SYM-H index (1d) shows an increase in ring current intensity from
 290 0500 UT while the ASYM-H index (1e) shows an increase in asymmetries in the ring cur-
 291 rent. Figure 1f shows the Kp index of between 1.7 and 2.3, which indicates minor ge-
 292 omagnetic activity during this period.

293 3.2 Radar Observations

294 Figure 2a shows the IMF Bz followed by panels presenting measurements of iono-
 295 spheric ion velocities for selected beams of the BKS SuperDARN radar between 0000-
 296 1000 UT, specifically beams 15 (b), 17 (c), 7 (d), 9 (e) and 17 (f) which are the beams
 297 that intersect through the FPI north, east, south, west and zenith assumed peak emis-
 298 sion locations respectively. Negative velocities indicate line of sight ion motion away from
 299 the radar and positive velocities towards the radar. The velocity magnitude is given by
 300 the colorbar on the right. Portions of the observations that have been determined to be
 301 groundscatter according the Ribeiro et al. (2011, 2012) algorithm have been marked in
 302 grey. The horizontal dashed lines across each beam range gate panel show the range gate
 303 where the assumed peak FPI emission point is located, calculated using the standard Su-
 304 perDARN virtual height model. Across all beam range gate panels we observe enhance-
 305 ments of the ion velocities during the southwards IMF Bz interval between 0400 and 0700

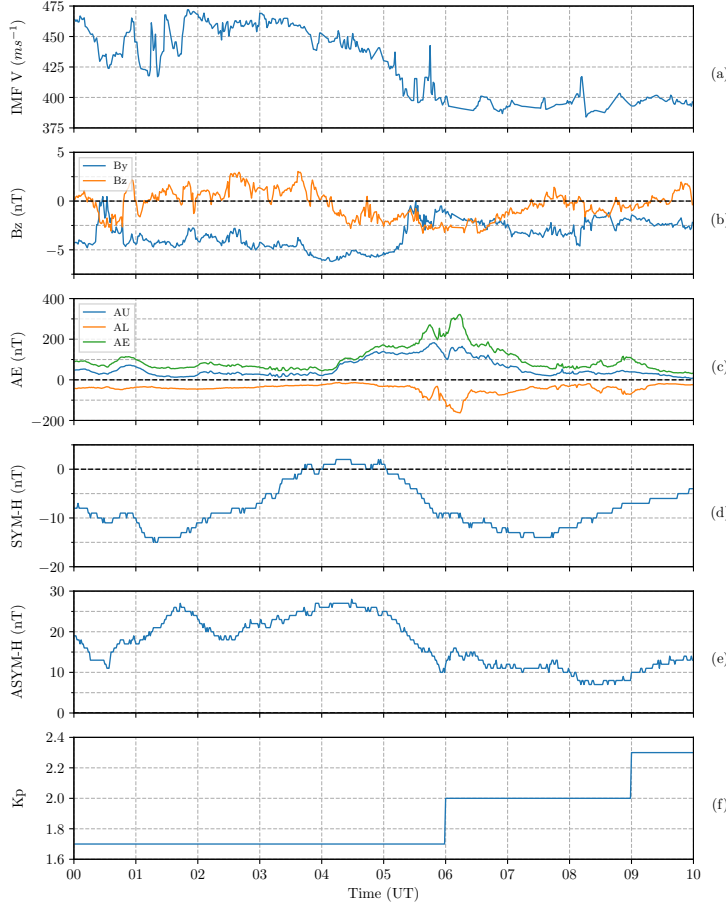


Figure 1. Geomagnetic conditions recorded during the nighttime interval (0000-1000 UT) of 16 July 2014. (a) Shows the IMF solar wind speed, v , (b) the IMF magnetic field strength in the y and z directions (c) the AU, AL and AE indices, (d) the SYM-H index, (e) the ASYM-H index and (f) the three hourly Kp index.

306 UT, with the most persistent flows traversing the southern and western part of the FPI
 307 region (panels d and e). The observed flows exceed -100 ms^{-1} . At high-latitudes, these
 308 flows may not be considered to be particularly strong, but at mid-latitudes and especially
 309 during periods of low geomagnetic activity such as this, these magnitudes particularly
 310 stand out from the background quiet time velocities of typically less than 20 ms^{-1} mag-
 311 nitude. Beams 15 and 17 show positive flows $> 40 \text{ ms}^{-1}$ between 0500 and 0600 UT close
 312 to the FPI (panels b and c) emission locations, indicating a change in flow direction dur-
 313 ing these periods, whereas beams 7 and 9 (panels d and e) show the line of sight ion ve-
 314 locities remaining strongly negative. The flow direction switch only in two adjacent beams
 315 indicates that multiple flow channels exist during this interval.

316 To illustrate the spatial morphology and geographical mapping of the excited ion
 317 flows, Figure 3 presents a snapshot of SuperDARN flow data from all the north Amer-
 318 ican mid-latitude radars from 0600 UT, superimposed with the Total Electron Content
 319 (TEC) and field-aligned currents (from AMPERE). The background of Figure 3 shows
 320 the $1^\circ \times 1^\circ$ geographic latitude by longitude height integrated TEC map, colored ac-
 321 cording to the white-black colorbar on the bottom. Dashed circles represent each 10° of
 322 geographic latitude. The AMPERE dataset shows the field aligned current densities, given

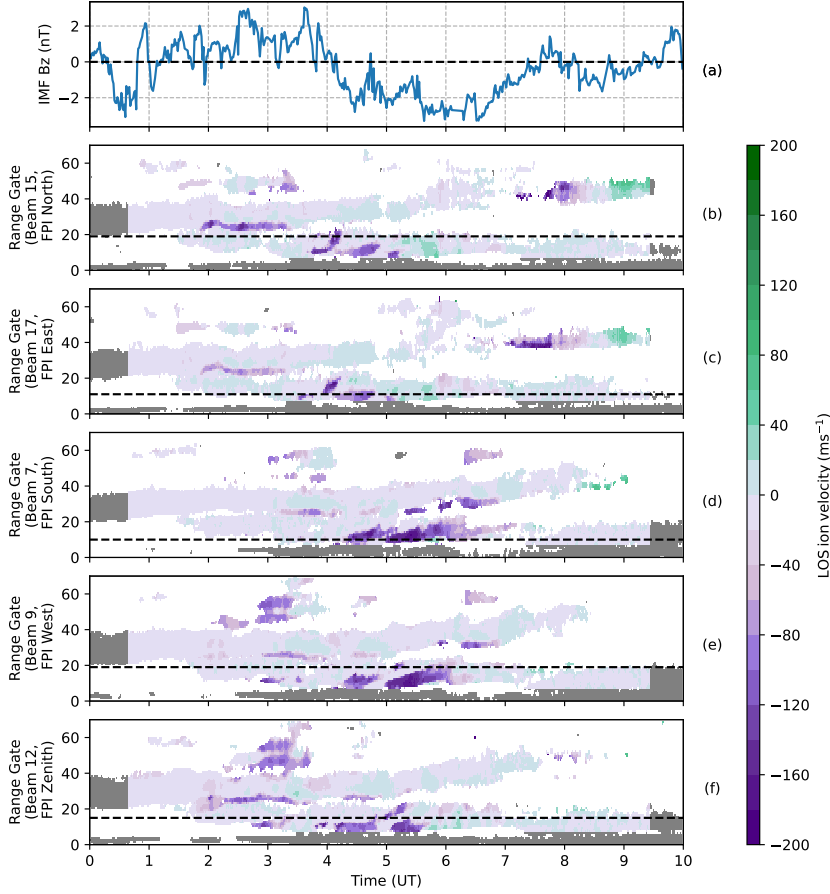


Figure 2. (a) shows the IMF Bz, followed by range gate, time plots for the BKS radar on 16 July 2014, with beams slicing through the assumed peak emission observation locations of the ANN FPI where beam 15 slices through north (b), 17 east (c), 7 south (d), 9 west (e) and 12 the zenith (f). Line of sight ion velocities follow the colorbar on the right, where positive values indicates motion towards the radar and negative away. Grey values are groundscatter. The dashed horizontal lines represent the range gate where the beam slices through the assumed cardinal peak emission of the ANN FPI.

323 by the blue-red colorscale; upward field aligned currents are in blue and downwards in
 324 red. Line of sight ion velocities from all the North American mid-latitude SuperDARN
 325 radars are plotted according to the purple-green colorbar, velocities $< |15|\text{ms}^{-1}$, which
 326 is the boundary for low/high velocity scatter in the Ribeiro et al. (2011) groundscatter
 327 algorithm, have been removed to improve visual clarity. Multiple radars are used in order
 328 to identify the spatial extent of the ionospheric scatter over the FPI, given as an orange
 329 box at around 85° west, 42° north, which traces the boundaries of the assumed peak
 330 neutral wind emission locations. The sign of the SuperDARN ion velocities have been
 331 altered from the presentation in figure 2 such that here positive velocities indicates east-
 332 wards directed ion flows and negative westwards.

333 Figure 3 corresponds to 0600 UT (0100 local time at the ANN FPI), chosen due
 334 to a strong westwards flow in the south-west region of the FPI area. By tracing a west-
 335 wards line that starts at $40^\circ\text{N} \sim 85^\circ\text{W}$ and finishes at $45^\circ\text{N} 105^\circ\text{W}$, we can see that the
 336 strong ion velocities close to the FPI persist through multiple ionospheric scatter ranges

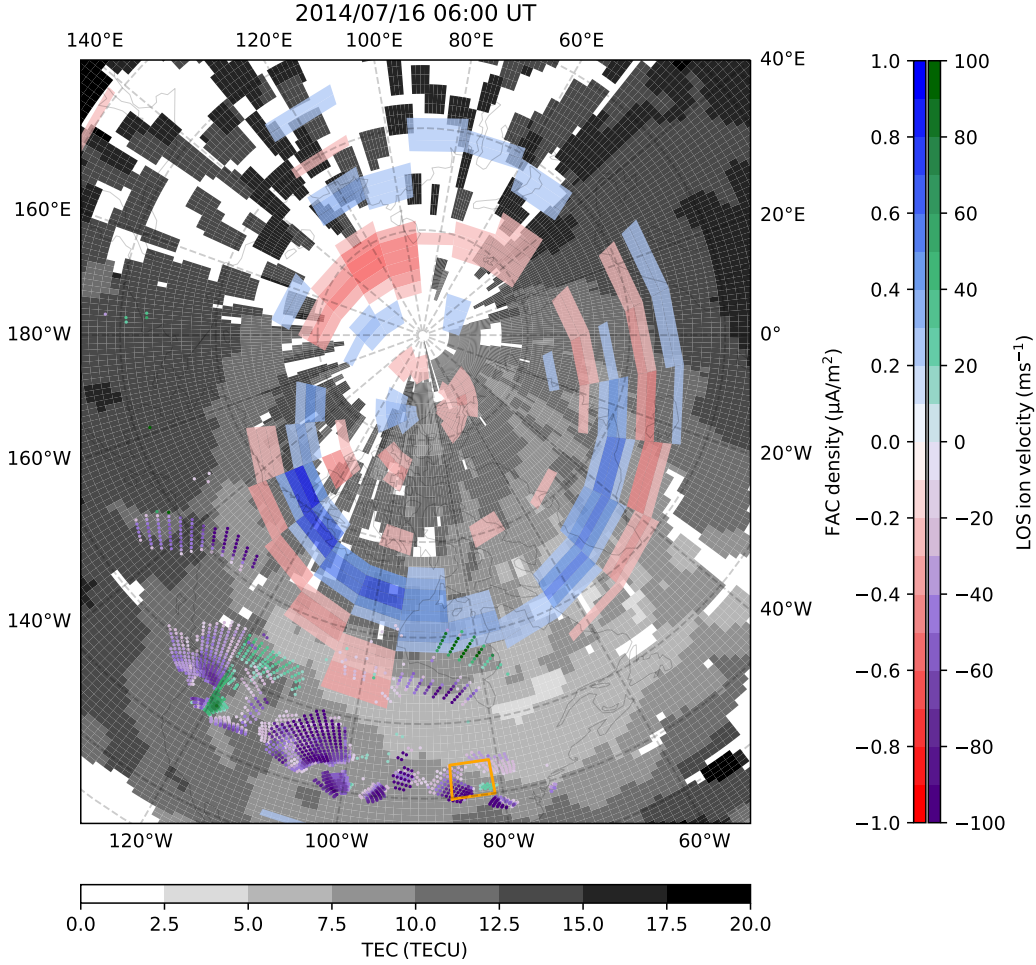


Figure 3. Geographic plot at 0600 UT 16 July 2016, showing the $1^\circ \times 1^\circ$ latitude \times longitude height integrated global total electron content according to the colorscale on the bottom. Dashed lines represent every 10° line of geographic latitude. Also shown is the AMPERE field aligned current density data, binned into 1° magnetic latitude by 1 hour MLT. Upward field aligned currents are given in blue and downwards in red with magnitude according to the red-blue colorbar. Further plotted are line of sight ion velocities from all the north American mid-latitude SuperDARN radars according to the purple-green colorbar, where absolute velocities $< 15\text{ms}^{-1}$ have been removed. Note that the line of sight SuperDARN ion velocities are colored so that positive values indicate an eastwards motion and negative a westwards directed flow. Plotted in orange is the box that bounds the FPI cardinal observation locations, where the FPI is located at 0100 local time in this Figure.

and into the FOV of more westwards located radars. The AMPERE dataset indicates that the R1/R2 boundary at midnight is between 60° and 50° geographic latitude, approximately 20° poleward of the FPI, we thus conclude that the observed flows are subauroral. From the TEC data we can see the formation of the ionospheric trough equatorward of the region 2 currents and poleward of the FPI, starting at $\sim 50^\circ$ geographic latitude at local midnight and wrapping around to $\sim 70^\circ$ geographic latitude at the dusk-side.

A more detailed presentation of the ion flow data from the BKS radar overlooking the ANN FPI is provided by figure 4, which shows the line of sight velocities for the BKS radar beam range gates that are assumed to contain the cardinal peak emission location of the FPI. Panels, a, b, c, and d are for the beams that slice through the north, south, east and west locations respectively at the range gate that contains the assumed peak emission location. Note, that the panels do not indicate that motion is north/south/east/westwards, instead positive values indicate motion towards the radar and negative away along the azimuth of the radar beam. The recorded line of sight ion velocities are indicated in blue. Shaded regions indicate the errors calculated using the method described in section 2. Compared in orange are the line of sight velocities from TIEGCM taken at an altitude of 250km at the same geographic latitude and longitude as the beam range gates and projected into the same direction as the radar beams.

The line of sight velocities show high activity across all beams between 0400 UT and 0700 UT. The northern and eastward observations show an early spike at 0400 UT with line of sight velocities of approximately 160ms^{-1} . The southern observations show several spikes of high velocities from 0400 to 0630 UT peaking at -180ms^{-1} slightly after 0530 UT. The westward observations show high velocity spikes occurring between 0500 and 0600 UT, peaking at slightly less than -150ms^{-1} . An interesting observation is that the IMF Bz was directed northwards until after 0400 UT, however the north and southward BKS radar line of sight measurements show strong flows from as early as 0330 UT, and the eastwards observation starts to spike just before 0400 UT, indicating some driver other than the IMF Bz contributed to the fast ion motion. Furthermore, we can see that the westwards spikes begin (~ 0510 UT) shortly after the strong eastwards observations end (~ 0445 UT), which could indicate that it is the same patch of scatter that traverses across the FOV of the radar. The TIEGCM line of sight resolved ion velocities follow the same general trend over each observation point. Differences between each region can be identified most notably at 0500 UT, where the east location is around -10ms^{-1} while the southern point has model velocities of $\sim -25\text{ms}^{-1}$. There are also slight variations in the magnitudes of the velocities due to the difference in the beam azimuth relative to TIEGCM's modelled three-dimensional ion flows. The TIEGCM line of sight ion velocities hover around their peak value of between $40-60\text{ms}^{-1}$ in all cells from roughly 0100 to 0300 UT, well before the first observed ion velocity spikes and southwards directed IMF Bz. They then decrease in velocity to close to 0ms^{-1} between 0500 UT (for the east observation point) and 0700 UT (for the south observation point).

3.3 FPI Observations

Figure 5 compares the FPI line of sight velocities (blue) with the neutral velocities modelled by TIEGCM at the assumed peak emission locations (orange). Panels a, b, c and d show the north, south, east and west observation directions respectively. Since TIEGCM's output velocities are given as geographic meridional and zonal magnitudes, we take TIEGCM's meridional flow for the north and south observations and the zonal flow for the east and west observations at each assumed peak emission location. We then project them into the same elevation angle as observed by the FPI. Positive velocities indicate motion to the north (meridionally) and east (zonally). The Zonal directions (east, west) show generally low velocities throughout the nighttime period, the meridional velocities however, show a gradual increase, particularly after the IMF Bz turns southward

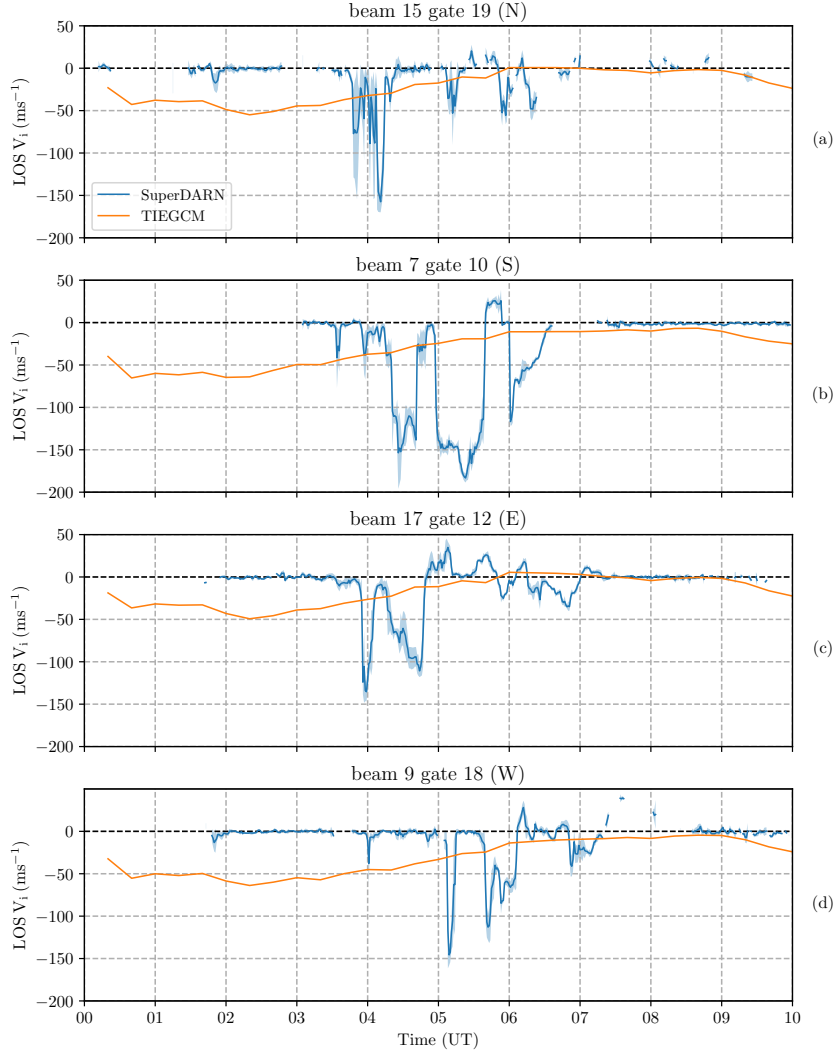


Figure 4. Line of sight ion velocities (blue) recorded from the BKS radar through 0000-1000 UT from the beam range-gate cells which overlay the ANN FPI assumed peak emission locations, north (a), south (b), east (c) and west (d). The overlaying FPI assumed peak emission locations for the cardinal directions are also indicated in each panel header. Positive values indicate motion towards the radar and negative away. Shaded regions indicate errors calculated by the method from Ruohoniemi and Baker (1998) but filtering out velocities two median absolute deviations from the median instead of two standard deviations from the mean. Also plotted are the equivalent line of sight ion velocities modelled by TIEGCM (orange).

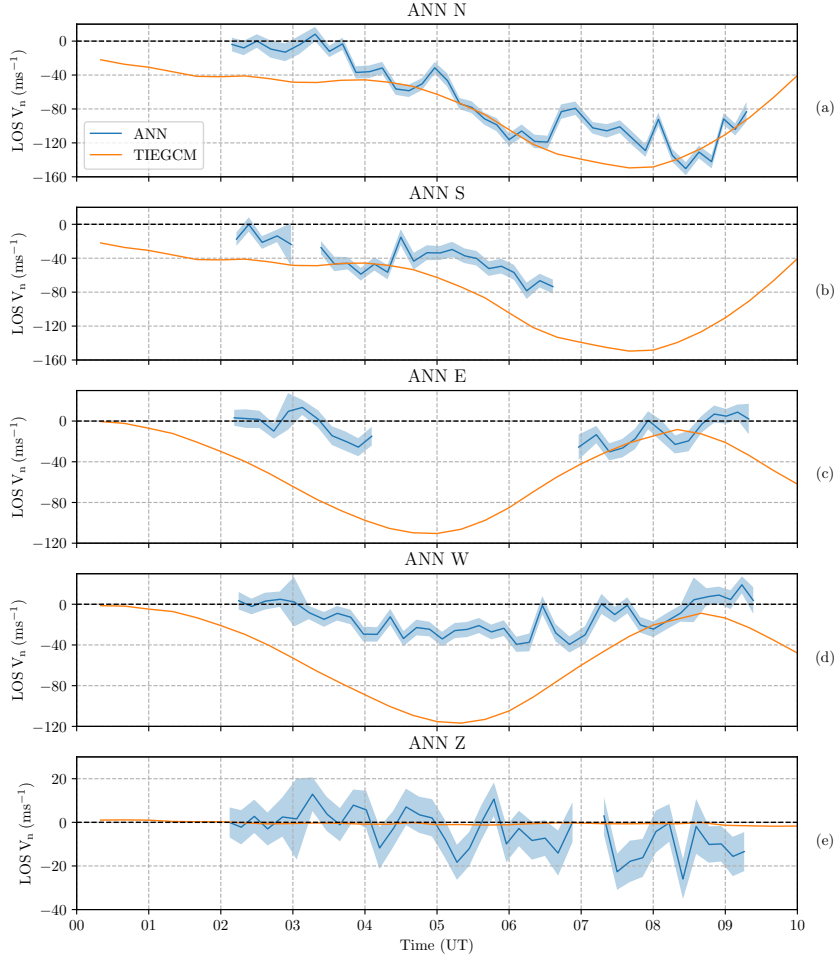


Figure 5. Line of sight neutral velocities recorded by the ANN FPI (blue) through 0000-1000 UT for each cardinal observation direction, north (a), south (b), east (c), west (d) and the vertical velocity measured by the zenith (e). Shaded regions show the error in the ANN observations. Positive velocities indicate motion north/east/upwards. Gaps are left where sequential measurements are made more than 20 minutes apart. Also plotted are the neutral velocities from TIEGCM for the equivalent line of sight locations and directions.

389 after 0500 UT. The north facing observations especially, show a large increase in mag-
 390 nitude up to a peak value of -150 ms^{-1} whereas the south facing observations peak at
 391 roughly -80 ms^{-1} . The zonal velocities show similar magnitudes with the East look di-
 392 rection peaking at -30 ms^{-1} and the west look direction at -40 ms^{-1} . Although in our
 393 ANN data, the south observations stop after 0630 UT and a 3 hour data gap occurs in
 394 the east observations between 0400 and 0700 UT due to the presence of the moon in that
 395 direction, the trend in the data between the opposing observation points are similar enough
 396 that we can assume that there are no significant changes in the spatial distribution of
 397 the neutral wind flows over the ANN FPI. The vertical velocities are shown to fluctu-
 398 ate highly relative to their greatest magnitude, ranging from values of 5 ms^{-1} to -20 ms^{-1} .

399 When comparing TIEGCM's output, we find that the modelled meridional veloc-
 400 ities are similar in magnitude to the observations. At the north location, TIEGCM's neu-
 401 tral velocities are closely aligned with these observations. TIEGCM's velocities at the
 402 southern location follow a similar pattern and although the observations stop after 0600
 403 UT, the trend of increasing magnitude from 0200 UT is apparent in both the observed
 404 and modelled data. The meridional velocities then match well with our observations. Both
 405 TIEGCM's velocities at the east and west locations are shown to have a large difference
 406 to the observations. Although the trend of a somewhat sinusoidal variation in both the
 407 observed and modelled neutral velocities between 0000 UT and 0900 UT, peaking at 0500
 408 UT, are somewhat similar, TIEGCM's velocities are significantly faster, especially at the
 409 peak. TIEGCM is more accurate when estimating the mid-latitude meridional neutral
 410 flows than in the zonal direction in this case.

411 4 Joule Heating Analysis

412 4.1 Methodology

413 Estimation of the Joule heating over the region requires at least the two-dimensional
 414 ion and neutral velocities for use in Equation 1. We use a technique similar to L-shell
 415 fitting (Villain et al., 1987; Ruohoniemi et al., 1989) which has been used for other mid-
 416 latitude ion studies (Clausen et al., 2012; Kunduri et al., 2018; Maimaiti et al., 2018, 2019),
 417 whereby the ion motion is assumed to be constant across some area. If such a flow is ob-
 418 served by a SuperDARN radar then the line of sight velocities vary azimuthally across
 419 the beams such that if a beam crosses the flow perpendicular to the flow direction it will
 420 return with a zero velocity. Conversely, if the beam is sounding in the direction parallel/anti-
 421 parallel to the full flow then it will return its full velocity. We can fit a cosine curve to
 422 the line of sight velocities against beam azimuth, where the magnitude of the fit provides
 423 the full 2D ion flow perpendicular to the magnetic field.

424 Initially a pre-defined area around the FPI was used where velocities in that area
 425 were selected and fit to a cosine curve, however this resulted in poor fits as it became
 426 apparent that there were multiple flow patches within the FPI region. Therefore, in or-
 427 der to accurately capture the dynamic ion motion over the FPI, we manually identified
 428 the individual ionospheric scatter patches, first by time-integrating the scans over pe-
 429 riods of 10 minutes to reduce temporal variability and then by marking the boundaries
 430 of each patch spatially and temporally. We then selected the highest magnitude veloc-
 431 ity from each beam within each defined patch and fit to those points. A minimum of five
 432 unique beams were used to constrain the fits, which although is less than used in other
 433 studies, e.g. Thomas and Shepherd (2018); Kunduri et al. (2018), manual (rather than
 434 automated) selection and review of the points ensures that they are still constrained to
 435 the fit. This further allowed deselecting beams at the sides of patches if by inspecting
 436 the fits it became clear that part the flow does not belong to the patch, ensuring that
 437 motion only belonging to that patch was captured.

438 Figure 6 shows an example of this fitting technique for the BKS scan from 0551
 439 to 0601 UT. The top panel shows the scan of line of sight ion velocities plotted onto a
 440 geographic grid with the ion velocities corresponding to the colorbar to the right. Pos-
 441 itive velocities indicate motion towards the radar, negative velocities away. Non-F-region
 442 ionospheric scatter or groundscatter identified by the Ribeiro algorithm has been col-
 443 ored grey. The location of the FPI is plotted at approximately 42° north, 84° west by
 444 the orange triangle. The assumed location of the peak neutral wind measurements are
 445 shown by the orange dots. The orange boxes mark what has been determined to be a
 446 patch of fast moving ionospheric scatter. Since we take the maximum velocity of each
 447 beam within a patch, it is only necessary to ensure that the highest velocity within a beam
 448 is included within the patch boundaries rather than needing to determine the exact spa-
 449 tial structure of the patch across all radar range gates. At the top right corner of each
 450 patch outline, a letter identifier (A, B, C, D and E) has been used to track each patch.
 451 At the time of the plot only patches C and D are present. Patches A and B occurred be-
 452 fore 0551 UT, while E after 0601 UT and so are not shown here. The two panels below
 453 show the highest line of sight ion velocities in each beam for both the patches outlined
 454 (C) and (D), plotted against their beam azimuths and the resulting cosine fits for each
 455 of those cells. A beam azimuth of 0° would point directly to magnetic north, negative
 456 azimuths indicate a westwards direction and positive eastwards. If we investigate the points
 457 used for fitting, patch C shows velocities that trend to positive at $+90^\circ$ azimuth, while
 458 patch D shows velocities that trend to a negative at $+90^\circ$ azimuth. Furthermore Patch
 459 C's eastmost beam and patch D's westmost beam show a difference of $\sim 150\text{ms}^{-1}$ within
 460 an azimuth range of only $10\text{-}15^\circ$. If both of these were included in the same fit, as would
 461 occur with a static fitting area, we would be unable to accurately fit it to a sinusoid. This
 462 analysis shows that points contained within C and D are therefore part of two separate
 463 patches of scatter. Therefore, by including the velocity-azimuth points and their fit re-
 464 sults in the patch determination process, we ensure that individual patches are accurately
 465 tracked.

466 By taking the fit magnitudes throughout the interval we are able to estimate the
 467 two dimensional ion flow during this period. Then by applying equation 2 with the IGRF
 468 magnetic field strength we can calculate the total local Joule heating across this inter-
 469 val. At high-latitudes, the quasi-vertical magnetic field results in the ion drift travel-
 470 ling approximately parallel to the Earth's surface in the same plane as the neutrals. How-
 471 ever, since the magnetic field is inclined (69.26° to the horizontal) at this latitude, the
 472 ions and neutrals reference planes are instead inclined roughly 20° relative to each other.
 473 The BKS radar only measures the ion velocity in the component perpendicular to \vec{B} , it
 474 is therefore necessary to mention that the derived fitted velocities may not be the rep-
 475 resentative of the full three dimensional ion velocities, but only the two dimensional ve-
 476 locities perpendicular to the magnetic field inclination. Due to the magnetic field incli-
 477 nation, it is also important that calculations of the coupling between the ions and neu-
 478 trals are made in the same plane relative to each other. As there is no estimate of the
 479 ion velocity in the direction parallel to the magnetic field, it is not possible to calculate
 480 the ion velocity in the plane horizontal to the Earth's surface. Since the FPI observes
 481 the geographic horizontal and vertical directions, the neutral wind velocity is obtainable
 482 fully in three-dimensions. By applying the three-dimensional rotation matrix transfor-
 483 mation given by equation 3,

$$\begin{bmatrix} N_{Bz} \\ N_{Bx} \\ N_{By} \end{bmatrix} = \begin{bmatrix} N_{mer} \\ N_{zon} \\ N_{ver} \end{bmatrix} \begin{bmatrix} \cos(\theta) & -\sin(\theta) & 0 \\ \sin(\theta) & \cos(\theta) & 0 \\ 0 & 0 & 1 \end{bmatrix} \begin{bmatrix} \cos(\phi) & 0 & \sin(\phi) \\ 0 & 1 & 0 \\ -\sin(\phi) & 0 & \cos(\phi) \end{bmatrix} \quad (3)$$

484 where N_{Bz} , N_{Bx} and N_{By} are the neutral wind components in the z , x , and y di-
 485 rections in magnetic field aligned coordinates respectively, and assuming the magnetic
 486 field is entirely in the z direction. N_{mer} , N_{zon} & N_{ver} are the geographic meridional, zonal

487 and vertical neutral wind components, θ is the angle subtended by the great circle lines
 488 connecting the FPI location to the geographic and magnetic north pole, while ϕ is the
 489 angle subtended between the magnetic field and the plane horizontal to Earth's surface
 490 at the location of the FPI.

491 As the observed neutral velocities are in the line of sight direction (45° inclination)
 492 of the FPI, we calculate the horizontal components of each cardinal observation, W_h , us-
 493 ing equation 4 (Makela et al., 2012),

$$W_h = \frac{W_{LOS} - W_v \sin(\alpha)}{\cos(\alpha)} \quad (4)$$

494 where W_{LOS} is the line-of-sight Doppler velocity, W_v is the vertical neutral veloc-
 495 ity and α is the elevation angle of the line of sight measurements. We assume that the
 496 zenith velocity measured above the FPI is consistent across the cardinal locations and
 497 so use that as the vertical velocity. The signs of the velocities are then changed such that
 498 positive velocities are directed northwards (meridionally). Because the FPI observations
 499 are made at different times with irregular cadences for each cardinal location, we linearly
 500 interpolate the observations so that the cadence of opposing east/west observations match.
 501 If only one opposing cardinal measurement is available at a given time, such as after 0600
 502 UT where no southwards observations were taken, we use the measurement we do have
 503 as the full meridional/zonal flow.

504 4.2 Results

505 Figure 7 shows IMF Bz (a) followed by the estimated observed (blue) and mod-
 506 elled (orange) magnitude of the full neutral wind vector (b). Figure 7c shows the fitted
 507 two dimensional ion velocities for each identified patch compared with those modelled
 508 by TIEGCM, while (d) shows the Pedersen conductivity, σ_p at the FPI location as mod-
 509 elled by TIEGCM and used for calculating the Joule heating. The solid lines represent
 510 the magnitude of the fitted velocity while the shaded region is the RMSE error of the
 511 fits. The largest RMSE is less than 20ms^{-1} , which given that the two major patches (B
 512 and C) are always at least 100ms^{-1} indicates that the fits to determine the two dimen-
 513 sional ion velocities are excellent. The time boundaries for the plot have been restricted
 514 to between 0400 and 0800 UT since no significant ion patches were identified either side
 515 of these times. The observed neutral's speed is seen to steadily increase from ~ 40 to
 516 $\sim 200\text{ms}^{-1}$ over the course of the night. TIEGCM overestimates the neutral velocities
 517 prior to 0600 UT, however afterwards, the total velocity magnitude is in line with the
 518 observations. Of the identified ion patches, two take precedence, patches B and C. Patch
 519 B appears at 0400 UT with velocities of 100ms^{-1} , increasing to in excess of 250ms^{-1} at
 520 0500 UT before dissipating. Patch C starts at 0500 UT, hovering at between 100 and
 521 200ms^{-1} until it also dissipates at 0700 UT. It is worth noting that the patches were only
 522 marked if they were at least covering part of the region within the FPI measurement lo-
 523 cations. It is likely that the patches originated or dissipated outside of this area and merely
 524 traversed through the region over the FPI, we have only noted the times where the patch
 525 is contained within the FPI region. Furthermore, patch A was identified to occur between
 526 0350 and 0420 UT, however the azimuthal span of the patch was not enough to satisfy
 527 the conditions we set in section 3 to fit a two-dimensional velocity, hence it is missing
 528 in this and further presentations of the patch ion velocities and Joule heating. TIEGCM's
 529 ion velocities remain a fairly steady $20\text{--}40\text{ms}^{-1}$ throughout the interval. As TIEGCM
 530 is a global large-scale model, it lacks the micro/mesoscale physics to capture the ion ir-
 531 regularities that produce the ion drift patches observed by the BKS radar, as evidenced
 532 here. The Pedersen conductivity is modelled to be relatively constant, although decreas-
 533 ing throughout the nighttime period.

534 Using the estimated two dimensional ion and neutral velocities, we have calculated
 535 the Joule heating rate and its components for each patch, assuming an altitude of 250km,
 536 plotted in Figure 8. Panels a, b, c, d and e show the Joule heating rate and components
 537 for patches A, B, C, D and E respectively. The blue line represents the ion heating rate,
 538 Q_i , the orange and green lines the two wind correction terms, Q_{w1} and Q_{w2} respectively
 539 and the red line the total Joule heating rate of the patch, calculated as the sum of the
 540 three components. A negative Q_{w1} indicates that the direction of the ion and neutrals
 541 were aligned with each other, resulting in fewer collisional interactions and thus damp-
 542 ening the overall heating rate, a positive value indicates the ions and neutrals were op-
 543 posed. Panel f shows the same components, but as modelled by TIEGCM. The final panel,
 544 g, compares the average total Joule heating rate from all the patches over the FPI re-
 545 gion, with the total heating rate modelled by TIEGCM. The TIEGCM Joule heating has
 546 been calculated by using its ion and neutral velocities for use in Equation 2, while keep-
 547 ing the other parameters the same as the observations, therefore the only difference be-
 548 tween the observed and modelled Joule heating rates, are the observed and modelled ion/neutral
 549 velocities. Based on the measurements, the most significant heating rate occurred be-
 550 tween 0430 and 0500 UT which resulted from ion motion from patch B, with heating due
 551 to ion motion, Q_i , peaking at roughly 236pWm^{-3} out of its total heating, Q_j , of 237pWm^{-3} .
 552 Patch C also exhibited some enhanced ion heating at 49.1pWm^{-3} , however this is some-
 553 what lower than the severe excitations in patch B.

554 The positive magnitude of Q_{w1} in patch C and D indicates that the ions and neu-
 555 trals were opposed in direction for most of each patch and so collisional interactions were
 556 increased. This increase is greatest in patch D at ~ 0520 UT, where the total heating
 557 is increased by 47pWm^{-3} to 109pWm^{-3} , resulting in a 78% increase due to the ion-neutral
 558 directions. The impact of this term is further shown in patch D, where at ~ 0550 UT,
 559 Q_{w1} is its most negative value and results in decreasing the total Joule heating by $\sim 76\%$.
 560 The heating directly due to the neutrals Q_{w2} is low throughout the entire interval, hov-
 561 ering at around $\sim 5\text{pWm}^{-3}$, therefore despite the large influence of the neutral wind di-
 562 rection on the total heating rate, the overall Joule heating magnitude is only significantly
 563 enhanced by ion motion.

564 The Joule heating enhancement observed in panel g at 0500 UT that peaked with
 565 a magnitude of 235pWm^{-3} is nearly 8 times higher than the TIEGCM modelled Joule
 566 heating of 30.8pWm^{-3} . Aside from ± 20 minutes of the 0500 UT peak, the TIEGCM
 567 Joule heating rate is significantly higher than the observational estimate. When we in-
 568 vestigate the reason behind the heating we find that the larger magnitudes in the ob-
 569 served ion heating, Q_i , especially in patch C, indicates that the observed heating is due
 570 to ion motion. Panel f shows that the magnitude of the total heating in TIEGCM is due
 571 to faster motion of the neutral winds, Q_{w2} , whose significance increases throughout the
 572 interval compared to the ion contribution. During this event, we find that our observa-
 573 tions disagree with not just the magnitude of the modelled Joule heating rate at the mid-
 574 latitudes, but the modelled Joule heating being from greater neutral wind motion dis-
 575 agrees with that calculated from our observations.

576 5 Discussion

577 The strong westwards driven ion flows that are observed in Figure 3 which persist
 578 through a longitude range of approximately 30° from 80°W to 110°W , could indicate
 579 that the flows captured in the FPI region are part of a SAPS. SAPS do not typically oc-
 580 cur during low geomagnetic activities, however Kunduri et al. (2017) found SAPS to oc-
 581 cur 15% of the time in the nightside during relatively quiet conditions with velocities \sim
 582 100ms^{-1} (Kunduri et al., 2018). Kunduri et al. (2021) also found SAPS latitudinal dis-
 583 tribution to correlate strongly with the ionospheric trough, which during this interval
 584 lies poleward of the FPI, suggesting that it would be unlikely for the flows to be a SAPS.
 585 Confirmation of the ion flows (not) being part of SAPS would require ion flux measure-

586 ments from satellite observations (Grocott et al., 2011; Clausen et al., 2012; Kunduri et
 587 al., 2017, 2018), however coincidental measurements were not available for the interval
 588 of this study. Instead we compare with findings from Kunduri et al. (2017), which stud-
 589 ied the latitudinal distribution of SAPS with correlation to the DST index. At 0600 UT
 590 (0030 MLT at the FPI location) the DST index was -1, which according to Kunduri et
 591 al. (2017), would place the mean SAPS position at 61° magnetic latitude ($\sim 51^\circ$ geo-
 592 graphic) with a minimum of 59° magnetic latitude ($\sim 49^\circ$ geographic), which would still
 593 be at least 7° poleward of the FPI location. Furthermore Nagano et al. (2015) calculated
 594 a quantitative estimation of the lower latitudinal boundary for SAPS keyed by SYM-H,
 595 which during this interval reached a minimum of -20nT. According to Nagano et al. (2015)
 596 this would result in a lower latitude boundary for SAPS of $\sim 58^\circ$ magnetic latitude (\sim
 597 48° geographic), still poleward of the FPI. We therefore suggest that the observations
 598 during this interval are not likely due to SAPS. If the ion enhancements are not due to
 599 high-latitude convection or to a SAPS, they may instead be part of a persistent quiet-
 600 time mid-latitude nighttime feature (Greenwald et al., 2006; Clausen et al., 2012) that
 601 appears due to pressure gradient instabilities often found at the equatorward boundary
 602 of the ionospheric trough (Hudson & Kelley, 1976; Greenwald et al., 2006; Liu et al., 2021),
 603 which would align spatially with our observations. While we suggest the ions to be pri-
 604 marily responsible for the increased Joule heating rates, we might expect currents to be
 605 present in the region of those Joule heating enhancements. However, there is no evidence
 606 of field-aligned currents at the FPI location, which is concerning and could be investi-
 607 gated further in future works. We do provide one possible explanation for the lack of FAC's
 608 in the region, which could be due to ions and electrons flowing in the same direction at
 609 250km altitude, potentially preventing any current from being produced.

610 Previous studies investigating mid-latitude nighttime ionospheric scatter have found
 611 ion velocities typically less than 100ms^{-1} (Greenwald et al., 2006; Maimaiti et al., 2018,
 612 2019). They are often attributed to penetrating electric fields, driven by the neutral wind
 613 dynamo or due to pressure gradient forces. Given the magnitude of Q_{w2} is small com-
 614 pared to the total Joule heating rate, Q_j , in this study, we infer that the ions are respon-
 615 sible for driving the increased Joule heating rate. Maimaiti et al. (2018, 2019) carried
 616 out statistical studies of the nightside mid-latitude and sub-auroral ionospheric convec-
 617 tion and found persistent westward flows between $20\text{--}90\text{ms}^{-1}$ depending on season and
 618 MLT, which is somewhat slower than our results, particularly as they found that the fastest
 619 flows occurred in winter. Although Maimaiti et al. (2018) used the same groundscatter
 620 algorithm (Ribeiro et al., 2011) as in this study to remove low velocity non-ionospheric
 621 scatter, they also deployed the additional technique as described in (Ribeiro et al., 2012),
 622 where events were only considered if the 3rd and 97th percentile of their ion velocity dis-
 623 tributions were greater than -120ms^{-1} and less than 120ms^{-1} respectively. This ensured
 624 that they only studied the quiet time mid-latitude nighttime scatter, however rare fast
 625 events may have been lost. By selecting active patches in this study, we have not con-
 626 sidered low-velocity ionospheric scatter during this event, this will have skewed our ve-
 627 locities to a higher range than theirs. We believe that the higher ion velocities estimated
 628 in this study are therefore reasonable. Furthermore, despite our ion velocities being greater
 629 than other quiet time studies, they are significantly slower than other mid-latitude stud-
 630 ies that occur under geomagnetically active periods. When enhanced ion velocities have
 631 been observed due to the equatorward expansion of auroral convection (Joshi et al., 2015)
 632 or SAPS (Clausen et al., 2012; Billett et al., 2022) velocities are observed in excess of
 633 500ms^{-1} and up to 1000ms^{-1} . Our observed ion velocities therefore fall within a rea-
 634 sonable expectation when considering the geomagnetic activity and methods used in this
 635 study.

636 Strong ion motion has been shown to drive the neutral atmosphere into a similar
 637 direction as momentum is exchanged through frictional collisions. During both patches
 638 C and D the directions of the ions and neutrals are initially opposed, resulting in an in-
 639 creased Joule heating rate, however as both patches persist, the neutrals are slowly driven

640 into the same direction as the ions, given by Q_{w1} decreasing. When the ion driving to
 641 the neutrals is at its greatest Q_{w1} would reach its peak negative value, and start to in-
 642 crease once the ion driving recedes and the neutrals retain momentum and start to drive
 643 the ions. In our observations Q_{w1} continues to decrease and never reach a negative peak
 644 over the tracked lifespan of both patches, with patch B lasting ~ 1.5 hours and patch
 645 C ~ 2 hours, suggesting the ions continue to drive the neutral motion throughout the
 646 period where we track them. Joshi et al. (2015) calculated the mid-latitude ion neutral
 647 coupling timescale during a geomagnetic storm and found a time-lag of ~ 84 minutes for
 648 the neutrals to respond to the ion driving. Billett et al. (2022) found a response time
 649 of 2h for mid-latitude neutral wind to respond to pressure gradient forces. In the case
 650 of Joshi et al. (2015), ions were driven by expanded auroral convection during a geomag-
 651 netic storm, and for Billett et al. (2022) a SAPS event, with ion velocities several 100ms^{-1}
 652 faster than this study's quiet time events. Kosch et al. (2001) found an average of high-
 653 latitude response times during geomagnetically quiet periods to be 3.3 hours. While we
 654 cannot calculate the full neutral coupling timescale because the neutrals never reach a
 655 steady state with the ions, the timescales in our observations can be viewed as the min-
 656 imum value for the coupling timescale. Our values are close to the full values from Joshi
 657 et al. (2015) and Billett et al. (2022), but are still smaller than those from the high-latitude
 658 timescales from Kosch et al. (2001), indicating that our values are reasonable.

659 Studies by Aruliah et al. (2005) and C. Anderson et al. (2013) investigated the im-
 660 pact that neutral winds have on Joule heating rate estimations. They calculated the high-
 661 latitude neutral wind dynamo to account for 29% (Aruliah et al., 2005) and 36% (C. An-
 662 derson et al., 2013) of the total Joule heating rates. Across patches B, C and D, the av-
 663 erage neutral contribution (Q_w) to the total heating rate was 24.7%, 40.4% and 43.1%
 664 respectively, which is consistent with the previous studies, albeit at different latitudes.
 665 Patch B's lower neutral contribution can be accounted for by the significantly stronger
 666 ion enhancements than in the other two patches, while their contributions although higher,
 667 still signify the majority of mid-latitude Joule heating response being due to the ions.
 668 Billett et al. (2018) indicated that the high-latitude Joule heating rate was nearly en-
 669 tirely eliminated when the neutral wind was pulled into the orientation of the ion flow.
 670 Kiene et al. (2019) used a scanning doppler imager with a SuperDARN radar to estimate
 671 high-latitude local Joule heating rates. They found that inclusion of the neutral winds
 672 in their Joule heating rate calculations dropped the total heating rate by a factor of \simeq
 673 3 at high-latitudes. At the minimum value of Q_{w1} , which occurred in patch D, the Joule
 674 heating rate was decreased from 24.1pWm^{-3} to 5.61pWm^{-3} , representing a 4.2 times
 675 decrease, similar to the observations found in Kiene et al. (2019). However, our obser-
 676 vations vary substantially with the winds either contributing positively or negatively to
 677 the total heating rate, amounting to either a $> |75\%|$ increase or reduction in the to-
 678 tal Joule heating rate depending on the neutral flow direction relative to the ions. When
 679 considering the multiplicative reduction, and the percentage decreases, our results show
 680 that the neutral winds have a significant reducing action on the overall Joule heating rate
 681 in line with the results obtained by the high-latitude studies of Billett et al. (2018); Kiene
 682 et al. (2019). Although these studies did not show cases of the neutrals increasing the
 683 heating, Aruliah et al. (2005) and C. Anderson et al. (2013) did find that high-latitude
 684 neutrals were able to enhance or reduce the total Joule heating rates as similarly shown
 685 in this study. The increased heating rate magnitude of $\sim 75\%$ in this study is symmet-
 686 rical to the heating magnitude when the neutrals were decreasing the heating rate, im-
 687 plying that the neutrals are equally effective at enhancing Joule heating rates as they
 688 are at dampening them.

689 Typically, studies investigating Joule heating rates calculate a height-integrated value
 690 using model values (McHarg et al., 2005; X. X. Zhang et al., 2005; Lu et al., 2016) or
 691 based on assumptions of the height integrated neutral pattern being representative of
 692 the neutral pattern at approximately 160km altitude (Billett et al., 2018) as shown by
 693 Lu et al. (1995), or by assuming that F-region altitude measurements map down to a

694 range of altitudes (Cai et al., 2014). Direct comparisons of our values to other studies
 695 are somewhat limited, however C. Anderson et al. (2013) and Kiene et al. (2019) calcu-
 696 lated high-resolution high-latitude local Joule-heating rates using instruments observ-
 697 ing the ions and neutrals at 250km, which provides an excellent comparison to our mid-
 698 latitude study. The Joule heating rate in this study peaks at $\sim 235\text{pWm}^{-3}$. Both C. An-
 699 derson et al. (2013) and Kiene et al. (2019) estimated the local high-latitude Joule heat-
 700 ing rates up to the order of nWm^{-3} for geomagnetically active intervals, an order of mag-
 701 nitude higher than our observations. The majority of their observations however were
 702 in the tens, or hundreds of pWm^{-3} , which matches our observations, suggesting small
 703 patches of ion scatter at mid-latitudes are able to produce local Joule heating enhance-
 704 ments similar to those observed at high-latitudes. Their most dominant Joule heating
 705 values were coincident with the auroral region, where ion velocities are typically much
 706 higher, often in excess of 1000ms^{-2} , particularly during geomagnetically intense peri-
 707 ods (such as in their studies). While we could compare our values with studies calcu-
 708 lating height-integrated Joule heating rates by assuming that the electric field maps to
 709 lower altitudes, the neutral wind measurements however do not, and doing so would in-
 710 troduce significant uncertainty into our calculations that we have attempted to avoid by
 711 keeping the ion and neutral measurements as co-located as possible. Nethertheless, they
 712 can be used as an insight into the difference between auroral and sub-auroral Joule heat-
 713 ing rates, which typically indicate higher magnitudes in the auroral region, with the dif-
 714 ference of at least an order of magnitude being fairly common (X. X. Zhang et al., 2005;
 715 Lu et al., 2016; Billett et al., 2018). Our values being an order of magnitude smaller than
 716 those in the high-latitude studies is reasonable. If we consider the fact that the high-latitude
 717 studies occurred during geomagnetically intense periods, while our mid-latitude study is
 718 during a quiet time period, our Joule heating values may be closer than expected, in-
 719 dicated that even small transient events can result in a significant Joule heating depo-
 720 sition in the mid-latitudes.

721 Baloukidis et al. (2023) compared statistical high-latitude Joule heating distribu-
 722 tions estimated by using the European incoherent scatter scientific association (EISCAT)
 723 radars with TIEGCM. Their EISCAT Joule heating estimations ranged from altitudes
 724 of 80 – 150km altitude and did not include the neutral wind contributions, so are not
 725 directly comparable to our estimations in this study, but their comparisons to TIEGCM
 726 are still useful. They found that during low Kp, TIEGCM’s modelled Joule heating was
 727 higher than their observed estimates. If we can assume that fast moving ion patches were
 728 averaged out in their low Kp statistical analysis, then our results of TIEGCM modelling
 729 higher Joule heating during low velocity ion events agrees with the findings from their
 730 study. At higher Kp, Baloukidis et al. (2023) also found TIEGCM’s observed Joule heat-
 731 ing was lower than their observed estimates. Although our study is a low Kp event, our
 732 periods of significant ion enhancements are more often associated with high levels of ge-
 733 omagnetic activity, so we can compare our fast moving ion patches to their high Kp anal-
 734 ysis, whereby we also agree that TIEGCM’s modelled Joule heating is lower than ob-
 735 served estimations. Similar to our findings, Baloukidis et al. (2023) remark that the dif-
 736 ference in their discrepancies between TIEGCM and their observations are due to small-
 737 scale effects that amount to sub-grid variability within TIEGCM that it cannot resolve.
 738 Due to this sub-grid variability, TIEGCM includes an empirically-derived multiplication
 739 factor named JOULEFAC to increase its internal Joule heating by a fixed factor of 1.5
 740 (NCAR, 2016) in order for its neutral temperatures to better agree with statistical ob-
 741 servations. One solution Baloukidis et al. (2023) propose is to adjust JOULEFAC with
 742 Kp so that different values are used for different levels of geomagnetic activity. Previ-
 743 ous studies have manually adjusted the value of JOULEFAC to better reproduce real-
 744 istic Joule heating values (Emery et al., 1999). Although there may be differences be-
 745 tween optimised JOULEFAC values for high and mid-latitudes, optimised JOULEFAC
 746 values may work on a statistical level, however it could not account for small scale spa-
 747 tial or temporal events such as in this study. A better JOULEFAC for low Kp may bring
 748 TIEGCM’s modelled Joule heating in line with our observed estimations for low veloc-

ity patches, however there would still be a large and potentially greater difference for excited ion motion, such as patch B between 0430 and 0500 UT in this study. Furthermore, adjusting JOULEFAC may "correct" the numerical Joule heating value, however it might not solve discrepancies between whether greater ion or neutral motion produces Joule heating as occurs in this study. Rather, if focusing on localised studies, improvements should be made for TIEGCM to better model the microscale electrodynamic of the mid-latitude ionosphere.

6 Conclusion

During the night of 16 July 2014 over mid-latitude North America the BKS SuperDARN radar observed highly localised ion velocity enhancements of over 200ms^{-1} while ANN FPI observed neutral velocities over 150ms^{-1} despite the lack of strong geomagnetic drivers. The use of combined AMPERE and TEC datasets shows the ion enhancements are sub-auroral, and likely driven by plasma gradient instabilities, a common quiet-time nighttime mid-latitude occurrence observed at the equatorward edge of the mid-latitude trough. The ion velocity increases drove significant Joule heating enhancements to the region, of a similar magnitude to results from high-latitude studies, with the maximum increases only a single order of magnitude less than under high-latitude geomagnetically active periods. The neutral wind was shown to have a significant impact on the overall heating rate, accounting for on average between 24% and 43% of the total heating, while at the extremes increasing or decreasing the total heating rate by in excess of 75%.

Comparisons with modelled ion and neutral velocities from TIEGCM indicate that TIEGCM does not model equivalent enhancements to the ion velocities due to being a large-scale model that does not include microscale electrodynamic processes, resulting in an approximate 8 times smaller modelled Joule heating rate than during the peak observed estimates. Although TIEGCM does a good job of modelling the meridional neutral velocities, the zonal velocities were an order of magnitude higher than our observations, enough to amplify the total neutral wind velocity such that the mid-latitude Joule heating reported by the model was due to greater motion of the neutrals rather than the ions as our observations suggest. The strong neutral wind in the model also resulted in a greater modelled Joule heating rate than our observational estimates during quieter periods of the interval.

Opportunities for studying mid-latitude ion-neutral coupling and the Joule heating response are rare and limited intervals exist with measurements from coincident instruments, particularly during quiet times to study such events, nevertheless further work is needed to better understand the dynamics of the mid-latitude ionosphere-thermosphere, especially during non-geomagnetically intense periods. Further understanding and better representation of the mid-latitude dynamics could help produce more accurate models for Joule heating predictions.

Open Research Section

All data used for this study are available from open-source from nonprofit organisations. The authors acknowledge the use of SuperDARN data. SuperDARN is a collection of radars funded by national scientific funding agencies of Australia, Canada, China, France, Italy, Japan, Norway, South Africa, United Kingdom, and United States of America, and we thank the international PI team for providing the data. The authors acknowledge access to the SuperDARN database via the British Antarctic Survey (<https://www.bas.ac.uk/project/superdarn/data>). Other data mirrors are hosted by the Virginia Tech SuperDARN group (<http://vt.superdarn.org/>) and the University of Saskatchewan (<https://superdarn.ca/data-download>). The radar data products used are the FI-TACF3.0 library and version 5.0 of the Radar Software Toolkit (RST) (Thomas et al.,

2022). The authors acknowledge use of NATION data, operated through support from the National Science Foundation and collaboration between the University of Illinois, the University of Michigan, Clemson University, Eastern Kentucky University, the Psigah Astronomical Research Institute, and Virginia Tech, NATION data can be found at the Madrigal Millstone Hill data repository (<http://millstonehill.haystack.mit.edu/index.html>). We thank the AMPERE team and the AMPERE Science Data Center for providing data products derived from the Iridium Communications constellation, enabled by support from the National Science Foundation, AMPERE data was obtained from <https://ampere.jhuapl.edu/browse/>. Data for TEC processing are provided from the following organizations: UNAVCO, Scripps Orbit and Permanent Array Center, Institut Geographique National, France, International GNSS Service, The Crustal Dynamics Data Information System (CDDIS), National Geodetic Survey, Instituto Brasileiro de Geografia e Estatística, RAMSAC CORS of Instituto Geográfico Nacional de la República Argentina, Arecibo Observatory, Low-Latitude Ionospheric Sensor Network (LISN), Topcon Positioning Systems, Inc., Canadian High Arctic Ionospheric Network, Centro di Ricerche Sismologiche, Système d’Observation du Niveau des Eaux Littorales (SONEL), RENAG: REseau NAtional GPS permanent, GeoNet the official source of geological hazard information for New Zealand, GNSS Reference Networks, Finnish Meteorological Institute, and SWEPOS Sweden. Access to these data are provided by madrigal network via: <http://cedar.openmadrigal.org/>. Data analysis and visualisations in this paper were generated using the free open-source software packages aacgm v2.6.2 (Shepherd, 2014; A. Burrell et al., 2020) and pyDarn version 3.1.1 (Martin et al., 2023). All solar wind data and geomagnetic indices were downloaded from NASA’s SPDF Coordinated Data Analysis Web (<https://cdaweb.gsfc.nasa.gov/index.html/>). The AE data are also available from the WDC for Geomagnetism, Kyoto (<http://wdc.kugi.kyoto-u.ac.jp/wdc/Sec3.html>) who prepared this index. The Kp index data resources are available at <https://www.gfz-potsdam.de/en/kp-index/>.

Acknowledgments

EKD acknowledges funding by the NERC doctoral grant NE/S007423/1. MTW and AG were funded by the UKRI NERC project NE/T000937/1. AG was funded by UKRI NERC projects NE/W003090/1 and NE/W003015/1. MTW was funded by UKRI STFC Ernest Rutherford Fellowship project ST/X003663/1. GL was supported in part by NASA LWS Program under award 80NSSC20K1784 and by NASA HSR Program under award 80NSSC21K1673. The National Center for Atmospheric Research is a major facility sponsored by the National Science Foundation under Cooperative Agreement No. 1852977. The authors would like to thank the National Science Foundation for awards AGS-6943256 and the Office of Naval research for award N00014-23-1-2160. We would like to thank J. J. Makela for providing NATION data and for useful discussions on its use. The Blackstone SuperDARN radar is maintained and operated by Virginia Tech under support by NSF grant AGS-1935110. TEC data is provided to the community by the Massachusetts Institute of Technology (MIT) under support from US National Science Foundation grant AGS-1952737. We gratefully acknowledge the use of The High End Computing facility at Lancaster University which has facilitated the necessary data processing for this study. TIEGCM simulation results have been provided by the Community Coordinated Modeling Center (CCMC) at Goddard Space Flight Center through their publicly available simulation services (<https://ccmc.gsfc.nasa.gov>).

References

- Alken, P., Thébault, E., Beggan, C. D., Amit, H., Aubert, J., Baerenzung, J., . . . Zhou, B. (2021, 12). International geomagnetic reference field: the thirteenth generation. *Earth, Planets and Space*, 73. doi: 10.1186/s40623-020-01288-x
- Anderson, B. J., Takahashi, K., & Toth, B. A. (2000, 12). Sensing global birkeland

- 850 currents with iridium engineering magnetometer data. *Geophysical Research*
 851 *Letters*, 27, 4045-4048. doi: 10.1029/2000GL000094
- 852 Anderson, C., Kosch, M. J., Nicolls, M. J., & Conde, M. (2013, 12). Ion-neutral
 853 coupling in earth's thermosphere, estimated from concurrent radar and opti-
 854 cal observations above alaska. *Journal of Atmospheric and Solar-Terrestrial*
 855 *Physics*, 105-106, 313-324. doi: 10.1016/j.jastp.2013.04.005
- 856 Anderson, P. C., Hanson, W. B., Heelis, R. A., Craven, J. D., Baker, D. N., &
 857 Frank, L. A. (1993, 4). A proposed production model of rapid subauroral ion
 858 drifts and their relationship to substorm evolution. *Journal of Geophysical*
 859 *Research: Space Physics*, 98, 6069-6078. doi: 10.1029/92ja01975
- 860 Aruliah, A. L., Griffin, E. M., Aylward, A. D., Ford, E. A. K., Kosch, M. J., Davis,
 861 C. J., ... Jussila, J. (2005). First direct evidence of meso-scale variability on
 862 ion-neutral dynamics using co-located tristatic fpis and eiscat radar in north-
 863 ern scandinavia (Vol. 23).
- 864 Baker, J. B., Zhang, Y., Greenwald, R. A., Paxton, L. J., & Morrison, D. (2004,
 865 5). Height-integrated joule and auroral particle heating in the night side
 866 high latitude thermosphere. *Geophysical Research Letters*, 31. doi:
 867 10.1029/2004GL019535
- 868 Baloukidis, D., Sarris, T., Tourgaidis, S., Pirnaris, P., Aikio, A., Virtanen, I.,
 869 ... Papadakis, K. (2023, 12). A comparative assessment of the distri-
 870 bution of joule heating in altitude as estimated in tie-gcm and eiscat over
 871 one solar cycle. *Journal of Geophysical Research: Space Physics*, 128. doi:
 872 10.1029/2023JA031526
- 873 Billett, D. D., Grocott, A., Wild, J. A., Walach, M. T., & Kosch, M. J. (2018, 3).
 874 Diurnal variations in global joule heating morphology and magnitude due to
 875 neutral winds. *Journal of Geophysical Research: Space Physics*, 123, 2398-
 876 2411. doi: 10.1002/2017JA025141
- 877 Billett, D. D., McWilliams, K. A., Kerr, R. B., Makela, J. J., Chartier, A. T., Ruo-
 878 honiemi, J. M., ... Riccobono, J. (2022, 9). Mid-latitude neutral wind re-
 879 sponses to sub-auroral polarization streams. *Annales Geophysicae*, 40, 571-583.
 880 doi: 10.5194/angeo-40-571-2022
- 881 Burrell, A., van der Meeren, C., & Laundal, K. M. (2020). aacgm2 [software]. doi:
 882 <https://zenodo.org/doi/10.5281/zenodo.1212694>
- 883 Burrell, A. G., Perry, G. W., Yeoman, T. K., Milan, S. E., & Stoneback, R. (2018,
 884 4). Solar influences on the return direction of high-frequency radar backscatter.
 885 *Radio Science*, 53, 577-597. doi: 10.1002/2017RS006512
- 886 Cai, L., Aikio, A. T., & Nygrén, T. (2014). Solar wind effect on joule heating in the
 887 high-latitude ionosphere. *Journal of Geophysical Research: Space Physics*, 119,
 888 10,440-10,455. doi: 10.1002/2014JA020269
- 889 Chisham, G., Lester, M., Milan, S. E., Freeman, M. P., Bristow, W. A., Grocott, A.,
 890 ... Walker, A. D. (2007, 1). A decade of the super dual auroral radar network
 891 (superdarn): Scientific achievements, new techniques and future directions
 892 (Vol. 28). doi: 10.1007/s10712-007-9017-8
- 893 Clausen, L. B., Baker, J. B., Ruohoniemi, J. M., Greenwald, R. A., Thomas, E. G.,
 894 Shepherd, S. G., ... Sazykin, S. (2012). Large-scale observations of a sub-
 895 auroral polarization stream by midlatitude superdarn radars: Instantaneous
 896 longitudinal velocity variations. *Journal of Geophysical Research: Space*
 897 *Physics*, 117. doi: 10.1029/2011JA017232
- 898 Cowley, S. W. H., & Lockwood, M. (1992). Excitation and decay of solar wind-
 899 driven flows in the magnetosphere-ionosphere system. *Copernicus*, 10, 103-
 900 115.
- 901 Coxon, J. C., Milan, S. E., & Anderson, B. J. (2018). A review of birkeland cur-
 902 rent research using ampere. In (p. 257-278). American Geophysical Union
 903 (AGU). Retrieved from [https://agupubs.onlinelibrary.wiley.com/](https://agupubs.onlinelibrary.wiley.com/doi/abs/10.1002/9781119324522.ch16)
 904 [doi: https://doi.org/10.1002/](https://doi.org/10.1002/doi/abs/10.1002/9781119324522.ch16)

- 9781119324522.ch16
- 905
906 Dang, T., Li, X., Luo, B., Li, R., Zhang, B., Pham, K., ... Wang, Y. (2022, 8).
907 Unveiling the space weather during the starlink satellites destruction event on
908 4 february 2022. *Space Weather*, 20. doi: 10.1029/2022SW003152
- 909 Dungey, J. W. (1961, 1). Interplanetary magnetic field and the auroral zones. *Phys.*
910 *Rev. Lett.*, 6, 47-48.
- 911 Emery, B. A., Lathuilere, C., Richards, P. G., Roble, R. G., Buonsanto, J., Knipp,
912 J., ... Niciejewski, R. (1999). Time dependent thermospheric neutral re-
913 sponse to the 2–11 november 1993 storm period. *Journal of Atmospheric and*
914 *Solar-Terrestrial Physics*, 61, 329-350. doi: 10.1016/S1364-6826(98)00137-0
- 915 Fang, T., Kubaryk, A., Goldstein, D., Li, Z., Fuller-Rowell, T., Millward, G., ...
916 Babcock, E. (2022, 11). Space weather environment during the spacex
917 starlink satellite loss in february 2022. *Space Weather*, 20. Retrieved from
918 <https://onlinelibrary.wiley.com/doi/10.1029/2022SW003193> doi:
919 10.1029/2022SW003193
- 920 Fuller-Rowell, T. J., Codrescu, M. V., Roble, R. G., & Richmond, A. D. (1997).
921 How does the thermosphere and ionosphere react to a geomagnetic storm? In
922 (p. 203-225). doi: 10.1029/GM098p0203
- 923 Greenwald, R. A., Baker, K. B., Dudeney, J. R., Pinnock, M., Jones, T. B., Thomas,
924 E. C., ... Yamagishi, H. (1995). Darn/superdarn. *Space Science Reviews*, 71,
925 761-796.
- 926 Greenwald, R. A., Oksavik, K., Erickson, P. J., Lind, F. D., Ruohoniemi, J. M.,
927 Baker, J. B. H., & Gjerloev, J. W. (2006, 9). Identification of the tem-
928 perature gradient instability as the source of decameter-scale ionospheric
929 irregularities on plasmopause field lines. *Geophysical Research Letters*, 33,
930 n/a-n/a. Retrieved from <http://doi.wiley.com/10.1029/2006GL026581>
931 doi: 10.1029/2006GL026581
- 932 Grocott, A., Milan, S. E., Baker, J. B., Freeman, M. P., Lester, M., & Yeoman,
933 T. K. (2011). Dynamic subauroral ionospheric electric fields observed by the
934 falkland islands radar during the course of a geomagnetic storm. *Journal of*
935 *Geophysical Research: Space Physics*, 116. doi: 10.1029/2011JA016763
- 936 Harding, B. J., Gehrels, T. W., & Makela, J. J. (2014, 2). Nonlinear regression
937 method for estimating neutral wind and temperature from fabry-perot inter-
938 ferometer data. *Appl. Opt.*, 53, 666-673. Retrieved from [https://opg.optica](https://opg.optica.org/ao/abstract.cfm?URI=ao-53-4-666)
939 [.org/ao/abstract.cfm?URI=ao-53-4-666](https://opg.optica.org/ao/abstract.cfm?URI=ao-53-4-666) doi: 10.1364/AO.53.000666
- 940 Heelis, R. A., Lowell, J. K., & Spiro, R. W. (1982). A model of the high-latitude
941 ionospheric convection pattern. *Journal of Geophysical Research*, 87, 6339. doi:
942 10.1029/ja087ia08p06339
- 943 Howell, D. C. (2005). Median absolute deviation. In (and ed.). John Wiley and
944 Sons, Ltd. Retrieved from [https://onlinelibrary.wiley.com/doi/abs/10](https://onlinelibrary.wiley.com/doi/abs/10.1002/0470013192.bsa384)
945 [.1002/0470013192.bsa384](https://onlinelibrary.wiley.com/doi/abs/10.1002/0470013192.bsa384) doi: <https://doi.org/10.1002/0470013192.bsa384>
- 946 Hudson, M. K., & Kelley, M. C. (1976). The temperature gradient drift instability
947 at the equatorward edge of the ionospheric plasma trough. *J Geophys Res*, 81,
948 3913-3918. doi: 10.1029/JA081i022p03913
- 949 Joshi, P. P., Baker, J. B. H., Ruohoniemi, J. M., Makela, J. J., Fisher, D. J., Hard-
950 ing, B. J., ... Thomas, E. G. (2015, 10). Observations of storm time mid-
951 latitude ion-neutral coupling using superdarn radars and nation fabry-perot
952 interferometers. *Journal of Geophysical Research A: Space Physics*, 120, 8989-
953 9003. doi: 10.1002/2015JA021475
- 954 Kiene, A., Bristow, W. A., Conde, M. G., & Hampton, D. L. (2019, 1). High-
955 resolution local measurements of f region ion temperatures and joule heating
956 rates using superdarn and ground-based optics. *Journal of Geophysical Re-*
957 *search: Space Physics*, 124, 557-572. doi: 10.1029/2018JA025997
- 958 Kilcommons, L. M., Redmon, R. J., & Knipp, D. J. (2017, 8). A new dmsp magne-
959 tometer and auroral boundary data set and estimates of field-aligned currents

- 960 in dynamic auroral boundary coordinates. *Journal of Geophysical Research: Space Physics*, 122, 9068-9079. doi: 10.1002/2016JA023342
- 961
- 962 Knipp, D. J., Emery, B. A., Engebretson, M., Li, X., McAllister, A. H., Mukai, T., ... Wilkinson, P. (1998, 11). An overview of the early november 1993 geomagnetic storm. *Journal of Geophysical Research: Space Physics*, 103, 26197-26220. doi: 10.1029/98ja00762
- 963
- 964
- 965
- 966 Knipp, D. J., Tobiska, W. K., & Emery, B. A. (2004). Direct and indirect thermospheric heating sources for solar cycles 21-23 (Vol. 224).
- 967
- 968 Kosch, M. J., Cierpka, K., Rietveld, M. T., Hagfors, T., & Schlegel, K. (2001, 4). High-latitude ground-based observations of the thermospheric ion-drag time constant. *Geophysical Research Letters*, 28, 1395-1398. doi: 10.1029/2000GL012380
- 969
- 970
- 971
- 972 Kunduri, B. S., Baker, J. B., Ruohoniemi, J. M., Coster, A. J., Vines, S. K., Anderson, B. J., ... Chartier, A. T. (2021, 10). An examination of magnetosphere-ionosphere influences during a saps event. *Geophysical Research Letters*, 48, doi: 10.1029/2021GL095751
- 973
- 974
- 975
- 976 Kunduri, B. S., Baker, J. B., Ruohoniemi, J. M., Nishitani, N., Oksavik, K., Erickson, P. J., ... Miller, E. S. (2018, 9). A new empirical model of the subauroral polarization stream. *Journal of Geophysical Research: Space Physics*, 123, 7342-7357. doi: 10.1029/2018JA025690
- 977
- 978
- 979
- 980 Kunduri, B. S., Baker, J. B., Ruohoniemi, J. M., Thomas, E. G., Shepherd, S. G., & Sterne, K. T. (2017, 6). Statistical characterization of the large-scale structure of the subauroral polarization stream. *Journal of Geophysical Research: Space Physics*, 122, 6035-6048. doi: 10.1002/2017JA024131
- 981
- 982
- 983
- 984 Lin, D., Wang, W., Garcia-Sage, K., Yue, J., Merkin, V., McInerney, J. M., ... Sorathia, K. (2022, 12). Thermospheric neutral density variation during the "spacex" storm: Implications from physics-based whole geospace modeling. *Space Weather*, 20. doi: 10.1029/2022SW003254
- 985
- 986
- 987
- 988 Liu, Y., Xiong, C., Wan, X., Lai, Y., Wang, Y., Yu, X., & Ou, M. (2021, 7). Instability mechanisms for the f-region plasma irregularities inside the mid-latitude ionospheric trough: Swarm observations. *Space Weather*, 19. doi: 10.1029/2021SW002785
- 989
- 990
- 991
- 992 Lu, G., Baker, D. N., McPherron, R. L., Farrugia, C. J., Lummerzheim, D., Ruohoniemi, J. M., ... Hayashi, K. (1998, 6). Global energy deposition during the january 1997 magnetic cloud event. *Journal of Geophysical Research: Space Physics*, 103, 11685-11694. doi: 10.1029/98ja00897
- 993
- 994
- 995
- 996 Lu, G., Emery, B. A., Rodger, A. S., Lester, M., Taylor, J. R., Evans, D. S., ... Chenette, D. L. (1996, 12). High-latitude ionospheric electrodynamics as determined by the assimilative mapping of ionospheric electrodynamics procedure for the conjunctive sundial/atlas 1/gem period of march 28-29, 1992. *Journal of Geophysical Research: Space Physics*, 101, 26697-26718. doi: 10.1029/96ja00513
- 997
- 998
- 999
- 1000
- 1001
- 1002 Lu, G., Richmond, A. D., Emery, B. A., & Roble, R. G. (1995). Magnetosphere-ionosphere-thermosphere coupling: Effect of neutral winds on energy transfer and field-aligned current. *Journal of Geophysical Research*, 100, 19643. doi: 10.1029/95ja00766
- 1003
- 1004
- 1005
- 1006 Lu, G., Richmond, A. D., Lühr, H., & Paxton, L. (2016, 7). High-latitude energy input and its impact on the thermosphere. *Journal of Geophysical Research: Space Physics*, 121, 7108-7124. doi: 10.1002/2015JA022294
- 1007
- 1008
- 1009 Maimaiti, M., Baker, J. B., Ruohoniemi, J. M., & Kunduri, B. (2019, 6). Morphology of nightside subauroral ionospheric convection: Monthly, seasonal, kp, and imf dependencies. *Journal of Geophysical Research: Space Physics*, 124, 4608-4626. doi: 10.1029/2018JA026268
- 1010
- 1011
- 1012
- 1013 Maimaiti, M., Ruohoniemi, J. M., Baker, J. B., & Ribeiro, A. J. (2018, 3). Statistical study of nightside quiet time midlatitude ionospheric convection.
- 1014

- 1015 Journal of Geophysical Research: Space Physics, 123, 2228-2240. doi:
1016 10.1002/2017JA024903
- 1017 Makela, J. J., Meriwether, J. W., Ridley, A. J., Ciocca, M., & Castellez, M. W.
1018 (2012). Large-scale measurements of thermospheric dynamics with a multisite
1019 fabry-perot interferometer network: Overview of plans and results from midlati-
1020 tude measurements (Vol. 2012). Hindawi Limited. doi: 10.1155/2012/872140
- 1021 Martin, C. J., Shi, X., Schmidt, M. T., Day, E. K., Bland, E. C., Khanal, K., ... K,
1022 J. K. (2023). pydarn [software]. doi: 10.5281/zenodo.7767590
- 1023 McHarg, M., Chun, F., Knipp, D., Lu, G., Emery, B., & Ridley, A. (2005). High-
1024 latitude joule heating response to imf inputs. Journal of Geophysical Research:
1025 Space Physics, 110. doi: 10.1029/2004JA010949
- 1026 Nagano, H., Nishitani, N., & Hori, T. (2015, 12). Occurrence characteristics
1027 and lowest speed limit of subauroral polarization stream (saps) observed
1028 by the superdarn hokkaido east radar. Earth, Planets and Space, 67. doi:
1029 10.1186/s40623-015-0299-7
- 1030 NCAR. (2016). Tiegcm documentation release 2.0 ncar high altitude observatory.
1031 Retrieved from [https://www.hao.ucar.edu/modeling/tgcm/tiegcm2.0/
1032 userguide/userguide.pdf](https://www.hao.ucar.edu/modeling/tgcm/tiegcm2.0/userguide/userguide.pdf)
- 1033 Nishitani, N., Ruohoniemi, J. M., Lester, M., Baker, J. B. H., Koustov, A. V., Shep-
1034 herd, S. G., ... Kikuchi, T. (2019, 12). Review of the accomplishments of
1035 mid-latitude super dual auroral radar network (superdarn) hf radars (Vol. 6).
1036 Springer Berlin Heidelberg. doi: 10.1186/s40645-019-0270-5
- 1037 Qian, L., Burns, A. G., Emery, B. A., Foster, B., Lu, G., Maute, A., ... Wang, W.
1038 (2014, 3). The ncar tie-gcm. In (p. 73-83). doi: 10.1002/9781118704417.ch7
- 1039 Ribeiro, A. J., Ruohoniemi, J. M., Baker, J. B., Clausen, L. B., Greenwald, R. A., &
1040 Lester, M. (2012). A survey of plasma irregularities as seen by the midlatitude
1041 blackstone superdarn radar. Journal of Geophysical Research: Space Physics,
1042 117. doi: 10.1029/2011JA017207
- 1043 Ribeiro, A. J., Ruohoniemi, J. M., Baker, J. B., Clausen, L. B., Larquier, S. D., &
1044 Greenwald, R. A. (2011). A new approach for identifying ionospheric backscat-
1045 ter in midlatitude superdarn hf radar observations. Radio Science, 46. doi:
1046 10.1029/2011RS004676
- 1047 Richmond, A. D., Ridley, E. C., & Roble, R. G. (1992). A thermosphere/ionosphere
1048 general circulation model with coupled electrodynamics. Geophysical Research
1049 Letters, 19, 601-604. doi: 10.1029/92GL00401
- 1050 Rideout, W., & Coster, A. (2006, 7). Automated gps processing for global total elec-
1051 tron content data. GPS Solutions, 10, 219-228. doi: 10.1007/s10291-006-0029
1052 -5
- 1053 Rishbeth, H. (1977). Drifts and winds in the polar f region. Journal of Atmospheric
1054 and Terrestrial Physics, 39, 111-116.
- 1055 Rishbeth, H., Moffett, R. J., & Bailey, G. J. (1969). Continuity of air motion in the
1056 mid-latitude thermosphere (Vol. 31). Pergamon Press.
- 1057 Ruohoniemi, J. M., & Baker, K. B. (1998, 9). Large-scale imaging of high-latitude
1058 convection with super dual auroral radar network hf radar observations. Jour-
1059 nal of Geophysical Research: Space Physics, 103, 20797-20811. doi: 10.1029/
1060 98ja01288
- 1061 Ruohoniemi, J. M., Greenwald, R. A., Baker, K. B., Villain, J.-P., Hanuise,
1062 C., & Kelly, J. (1989). Mapping high-latitude plasma convection with
1063 coherent hf radars. Journal of Geophysical Research, 94, 13463. doi:
1064 10.1029/ja094ia10p13463
- 1065 Shepherd, S. G. (2014). Altitude-adjusted corrected geomagnetic coordinates: Defi-
1066 nition and functional approximations. Journal of Geophysical Research: Space
1067 Physics, 119, 7501-7521. doi: 10.1002/2014JA020264
- 1068 Thomas, E. G., Baker, J. B., Ruohoniemi, J. M., Clausen, L. B., Coster, A. J.,
1069 Foster, J. C., & Erickson, P. J. (2013, 3). Direct observations of the role of

- 1070 convection electric field in the formation of a polar tongue of ionization from
 1071 storm enhanced density. *Journal of Geophysical Research: Space Physics*, 118,
 1072 1180-1189. doi: 10.1002/jgra.50116
- 1073 Thomas, E. G., Reimer, A. S., Bland, E. C., Burrell, A. G., Grocott, A., Pono-
 1074 marenko, P. V., ... Walach, M.-T. (2022). Superdarn radar software toolkit
 1075 (rst) [software]. doi: <https://zenodo.org/doi/10.5281/zenodo.801458>
- 1076 Thomas, E. G., & Shepherd, S. G. (2018, 4). Statistical patterns of ionospheric con-
 1077 vection derived from mid-latitude, high-latitude, and polar superdarn hf radar
 1078 observations. *Journal of Geophysical Research: Space Physics*, 123, 3196-3216.
 1079 doi: 10.1002/2018JA025280
- 1080 Vasyliunas, V. M., & Song, P. (2005). Meaning of ionospheric joule heating. *Journal*
 1081 *of Geophysical Research: Space Physics*, 110. doi: 10.1029/2004JA010615
- 1082 Vierinen, J., Coster, A. J., Rideout, W. C., Erickson, P. J., & Norberg, J. (2016,
 1083 3). Statistical framework for estimating gnss bias. *Atmospheric Measurement*
 1084 *Techniques*, 9, 1303-1312. doi: 10.5194/amt-9-1303-2016
- 1085 Villain, J. P., Greenwald, R. A., Baker, K. B., & Ruohoniemi, J. M. (1987). Hf
 1086 radar observations of e region plasma irregularities produced by oblique
 1087 electron streaming. *Journal of Geophysical Research*, 92, 12327. doi:
 1088 10.1029/ja092ia11p12327
- 1089 Wahlund, J. E., Opgenoorth, H. J., Häggström, I., Winser, K. J., & Jones, G. O. L.
 1090 (1992, 3). Eiscat observations of topside ionospheric ion outflows during au-
 1091 roral activity: Revisited. *Journal of Geophysical Research: Space Physics*, 97,
 1092 3019-3037. doi: 10.1029/91ja02438
- 1093 Walach, M. T., & Grocott, A. (2019). Superdarn observations during geomag-
 1094 netic storms, geomagnetically active times, and enhanced solar wind driv-
 1095 ing. *Journal of Geophysical Research: Space Physics*, 124, 5828-5847. doi:
 1096 10.1029/2019JA026816
- 1097 Walach, M. T., Grocott, A., & Milan, S. E. (2021, 4). Average ionospheric elec-
 1098 tric field morphologies during geomagnetic storm phases. *Journal of Geophys-
 1099 ical Research: Space Physics*, 126. doi: 10.1029/2020JA028512
- 1100 Wang, X., Miao, J., Aa, E., Ren, T., Wang, Y., Liu, J., & Liu, S. (2020, 8). Sta-
 1101 tistical analysis of joule heating and thermosphere response during geomag-
 1102 netic storms of different magnitudes. *Journal of Geophysical Research: Space*
 1103 *Physics*, 125. doi: 10.1029/2020JA027966
- 1104 Weimer, D. R. (2005). Improved ionospheric electrodynamic models and applica-
 1105 tion to calculating joule heating rates. *Journal of Geophysical Research: Space*
 1106 *Physics*, 110. doi: 10.1029/2004JA010884
- 1107 Wu, Q., Jee, G., Lee, C., Kim, J. H., Kim, Y. H., Ward, W., & Varney, R. H. (2017,
 1108 1). First simultaneous multistation observations of the polar cap thermospheric
 1109 winds. *Journal of Geophysical Research: Space Physics*, 122, 907-915. doi: 10
 1110 .1002/2016JA023560
- 1111 Zhang, S. R., Erickson, P. J., Zhang, Y., Wang, W., Huang, C., Coster, A. J.,
 1112 ... Kerr, R. (2017, 1). Observations of ion-neutral coupling associated
 1113 with strong electrodynamic disturbances during the 2015 st. patrick's day
 1114 storm. *Journal of Geophysical Research: Space Physics*, 122, 1314-1337. doi:
 1115 10.1002/2016JA023307
- 1116 Zhang, X. X., Wang, C., Chen, T., Wang, Y. L., Tan, A., Wu, T. S., ... Wang, W.
 1117 (2005). Global patterns of joule heating in the high-latitude ionosphere. *Jour-
 1118 nal of Geophysical Research: Space Physics*, 110. doi: 10.1029/2005JA011222
- 1119 Zou, Y., & Nishitani, N. (2014, 8). Study of mid-latitude ionospheric convection dur-
 1120 ing quiet and disturbed periods using the superdarn hokkaido radar. *Advances*
 1121 *in Space Research*, 54, 473-480. doi: 10.1016/j.asr.2014.01.011

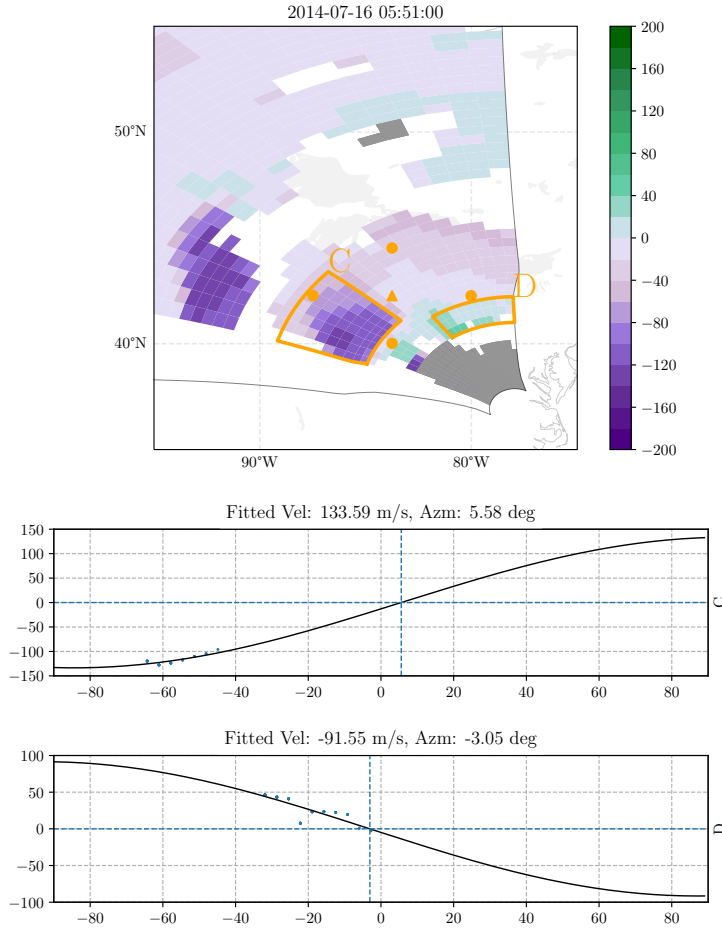


Figure 6. Example 10-minutely integrated scan starting from 0551 UT of the BKS radar on 16 July 2014, plotted on a geographic map in the top panel. Ion velocities are color coded according to the colorbar on the right, where positive velocities indicate motion towards the radar and negative away. Non-ionospheric scatter as marked by the Ribeiro algorithm is colored grey. The orange triangle represents the location of the ANN FPI, and the orange dots mark the assumed peak neutral wind measurement locations. Outlined in orange with labels are patches identified as C and D. Patches A, B, E are not present at the time of the plot. Below shows the line of sight ion velocities plotted as blue dots against their beam azimuth for each patch outlined in orange and marked with with the letter label. The black line represents the least-squares sinusoidal fit where the magnitude of the fit, and azimuth where the fit returns zero is given above each plotting box.

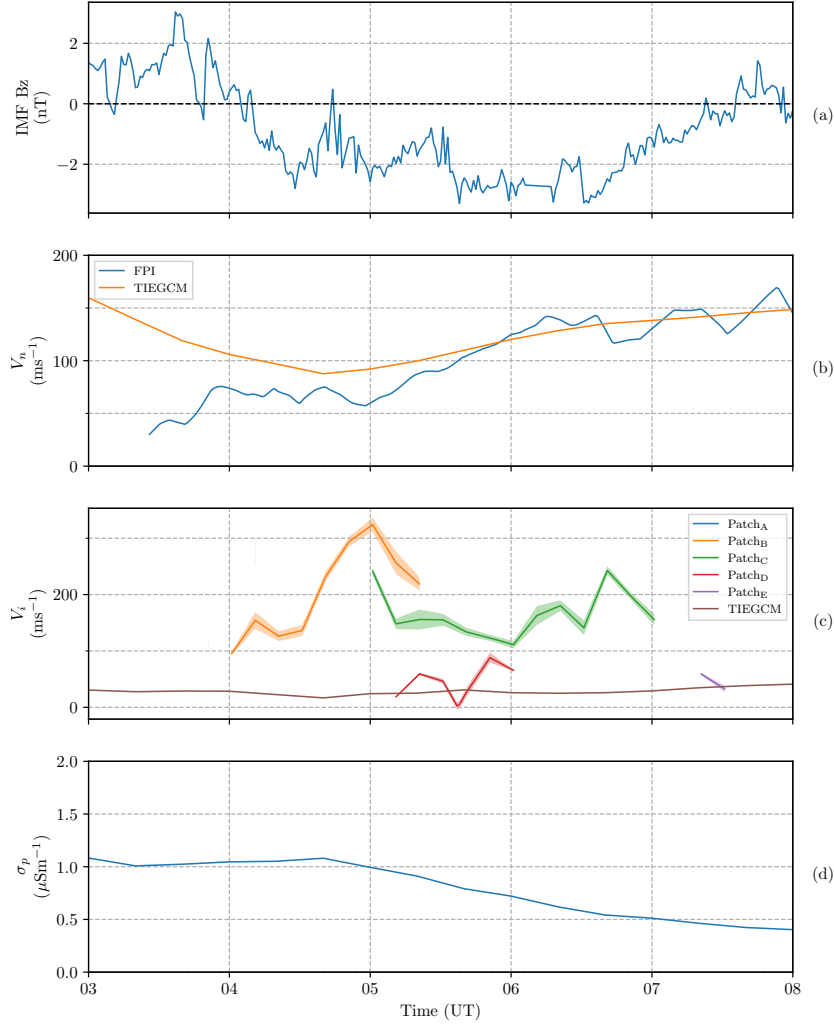


Figure 7. (a) IMF B_z followed by, (b) the magnitude of the full neutral wind vector in blue with TIEGCM's neutral velocities in orange, (c) the magnitude of the full ion velocities for each identified patch. The dark lines represent the fitted values, the shaded region either side of the line shows the root mean squared error (RMSE) of the fit used to estimate the velocity. The TIEGCM ion velocities are plotted as the burgundy line without a RMSE shaded region. (d) Shows the Pedersen conductivity at the FPI location, as modelled by TIEGCM.

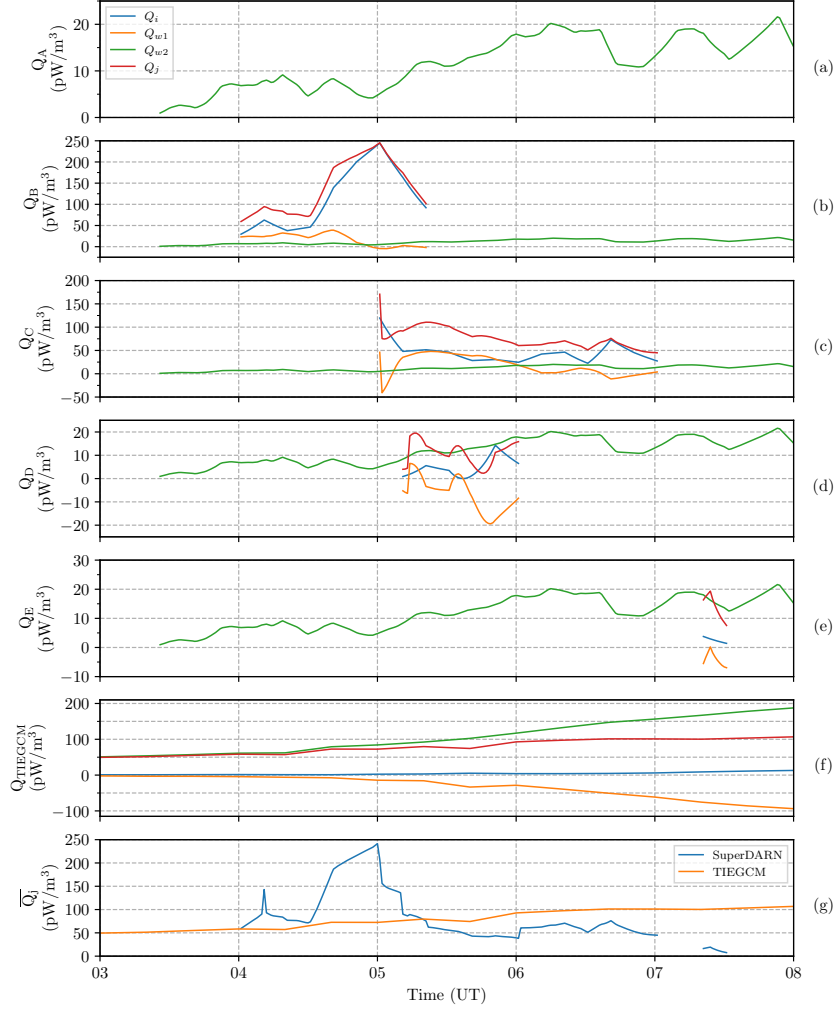


Figure 8. Panels a, b, c, d & e shows The estimated Joule heating components and total heating for each identified patch, the panel labels correspond to the patch velocity labels shown in figure 7c. Each component is plotted according to the legend in panel a. Panel f shows the Joule heating components and total heating modelled by TIEGCM. g shows the total Joule heating rate calculated as the average heating rate of all patches in the common area, while re-plotting TIEGCM's total Joule heating in orange for comparison.